

## ABSTRACT

Title of Thesis:       **EVALUATING A FEMTOSECOND LASER-  
INDUCED BREAKDOWN SPARK AS AN  
AERO-OPTIC ILLUMINATION SOURCE**

**Christoph Neisess  
Master of Science, 2022**

Thesis Directed by: **Professor Christopher Cadou  
Department of Aerospace Engineering**

Currently, limitations exist on collecting aero-optic wavefront data in a wind tunnel due to the types of sources available to illuminate the flow-field for the sensing optics. Collimated laser sources are commonly used, but are limited by the ability to place hardware to steer the beam towards the sensing optics. Laser-Induced Breakdown (LIB) sparks have also been tested, but create additional measurement errors due to variations in their size and position with each laser pulse. In this work, a new approach using a Femtosecond Laser-Induced Breakdown (FS-LIB) spark is evaluated as a possible solution to the problems faced by nanosecond LIB sparks, namely the significant amount of spark size and position variation present in the latter. The FS-LIB spark was imaged with a camera in order to study the amount of pulse-to-pulse position and size change present in its generation. Additionally, the FS-LIB spark was used to collect aero-optic data in conjunction with a Shack-Hartmann style wavefront sensor on a Mach 2.8 flowfield. The results of this analysis indicated that the FS-LIB spark experiences significantly

less pulse-to-pulse variation in its size and position than a nanosecond LIB spark. In addition, the wavefront data collected with the FS-LIB spark compared favorably to data collected with a more conventional collimated laser beam for illumination. This indicates that the FS-LIB spark is a promising alternative to the use of collimated sources in aero-optic data collection.

EXAMINING A FEMTOSECOND LASER-INDUCED BREAKDOWN  
SPARK AS AN AERO-OPTIC ILLUMINATION SOURCE

by

Christoph Richard Neisess

Thesis submitted to the Faculty of the Graduate School of the  
University of Maryland, College Park in partial fulfillment  
of the requirements for the degree of  
Master of Science  
2022

Advisory Committee:

Professor Christopher Cadou, Chair/Advisor  
Professor Kenneth Yu  
Professor Stuart Laurence  
Professor Kenneth Kiger

© Copyright by  
Christoph Neisess  
2022

## Acknowledgments

I owe many thanks to a number of people that have been involved in my graduate studies, both directly and indirectly. Without you all my graduate education would not have been a success.

I would like to thank my advisor, Dr. Christopher Cadou, for always providing ideas and insight to continually improve the quality of my research, and for helping me locate references to understand the topics my research delved into that I did not have significant background in. The quality of the following work would not have been possible without you.

I would also like to thank Dr. Brianne McManaman for serving as my mentor in the field of aero-optics. I lost count of how many times you helped me puzzle out a problem with my data reduction code or troubleshoot my experimental setup, and I deeply appreciate the time you spent helping me understand the major aspects of my research and showing me how to collect and process high-quality data for my thesis.

I would also like to thank Dr. Mark Rennie for providing helpful insight into the prior research conducted on breakdown sparks and for feedback on my experimental setup.

I would also like to thank the entire staff at AEDC Hypervelocity Wind Tunnel 9 for supporting me through my graduate journey and assisting me with everything I needed to put together the experiment I performed in the work presented here.

I would like to thank my family and friends as well for always being supportive of my

endeavors, and keeping me sane when I was struggling to reach milestones in my research or complete difficult coursework.

For those I have left out, I apologize for your omission. I would like to thank you as well for your help and support during my graduate journey.

# Table of Contents

Acknowledgements	ii
Table of Contents	iv
List of Tables	vi
List of Figures	vii
Chapter 1: Introduction	1
1.1 Motivation	1
1.2 Prior Research	6
1.2.1 Current and Previous Aero-Optics Testing	6
1.2.2 Wavefront Data Processing	9
1.2.3 Aero-Optic Guide Stars	11
1.2.4 FS-LIB	14
1.3 Objectives	16
1.4 Approach	16
Chapter 2: Methodology	18
2.1 Experimental Setup	18
2.2 Run Matrix	25
2.3 Data Collection Process	27
2.4 Data Reduction Process	28
2.5 Uncertainty Analysis	32
Chapter 3: Results: Spark Analysis	33
3.1 FS-LIB Spark Size and Shape	33
3.2 Wavefront Tip and Tilt	39
3.3 Spark Dimension Change with Pressure	43
Chapter 4: Results: Spark Wavefront Analysis	47
4.1 Spark Wavefronts	47
4.2 Comparisons to Collimated Laser Wavefronts	52
4.3 Spark Wavefront Modal Analysis	58
4.4 Comparisons to ND Model	61
Chapter 5: Conclusions and Future Work	63

5.1	Conclusions	63
5.2	Future Work	65
	Appendix A: MATLAB Code	66
	Bibliography	89

## List of Tables

2.1	A Summary of M3T Flow Properties . . . . .	19
3.1	Spark Centroid Motion in the X and Y Axes . . . . .	37
3.2	Average Tip and Tilt Magnitudes (Wind On) . . . . .	40
3.3	Spark Centroid Motion to Wavefront Tip/Tilt Correlation Strength by Run . . . . .	43

## List of Figures

1.1	An Illustration of How Flow Features Can Alter a Sensor’s View of an Object . . .	2
1.2	An Illustration of the Change in Wavefront Shape Due to Flow Features . . . . .	4
1.3	An Illustration of a Test Article in a Wind Tunnel with Two Viewing Angles Shown Along with a Collimated Laser Source for Illumination . . . . .	5
1.4	Illustration of the Shack-Hartmann Sensor Operation . . . . .	9
2.1	The Tunnel 9 Aero Cal Lab and Mach 3 Tunnel (M3T) . . . . .	18
2.2	The Test Section of the M3T with the Blunt Body Installed . . . . .	21
2.3	The FS-LIB Spark . . . . .	22
2.4	Optical Diagram Showing Both the Collimated Source and FS-LIB Spark Paths .	24
2.5	The Two Cameras Used to Collect Data on the Spark. On the Left is the Microlens Array Mounted in the Intensified Camera and on the Right is the IDT Camera with Zoom Lens . . . . .	25
2.6	The Run Matrix Showing all Runs Used for the Present Work . . . . .	27
2.7	The Main Steps in the Wavefront Data Reduction Process. 1) Subaperture Generation, 2) Spot Centroid Location, 3) Mean-Subtracted Wavefront Generation, 4) Tip/Tilt Removal to Reveal Turbulent Features . . . . .	31
3.1	The FS-LIB Spark as Seen on the IDT Camera . . . . .	34
3.2	The Norm of the Displacement of the Spark Centroid from the Mean Image over the Course of One Run . . . . .	36
3.3	The Percent Width Change of the Spark from the Mean Image over the Course of One Run . . . . .	38
3.4	The Percent Height Change of the Spark from the Mean Image over the Course of One Run . . . . .	38
3.5	The Percent Area Change of the Spark from the Mean Image over the Course of One Run . . . . .	39
3.6	The Wavefront Tip and Tilt Present Before a Run Using the FS-LIB Spark . . . .	40
3.7	The Wavefront Tip and Tilt Present During One Run Using the FS-LIB Spark . .	41
3.8	The Relationship Between Wavefront Tip and Spark Centroid X-Displacement . .	42
3.9	The Relationship Between Wavefront Tilt and Spark Centroid Y-Displacement . .	43
3.10	The FS-LIB Spark Generated at Various Ambient Pressures. From left to right: 760 torr, 100 torr, and 10 torr. . . . .	44
3.11	The FS-LIB Spark Dimension Change with Pressure . . . . .	45
3.12	The FS-LIB Spark Average Centroid Displacement Versus Pressure . . . . .	46

4.1	An Example of the Raw Wavefront Sensor Images . . . . .	48
4.2	Examples of Instantaneous Wavefronts Imaged With the Spark. The Wind-On Wavefront Shows Additional Distortions that Could be Related to Boundary Layer Turbulence . . . . .	50
4.3	An Example Time Trace of $OPD_{rms}$ During Tunnel Startup and Good Flow of an Empty Tunnel Run with a Moving Average Overlaid . . . . .	51
4.4	An Example Time Trace of $OPD_{rms}$ for Startup, Good Flow, and Unstart of an Extended Run with the Blunt Body Installed in the Tunnel . . . . .	52
4.5	An Example Comparison of $OPD_{rms}$ Time Traces . . . . .	53
4.6	A Comparison of the FS-LIB Spark and CW Source $OPD_{rms}$ Moving Averages (Tunnel Start-Up) . . . . .	54
4.7	A Comparison of the FS-LIB Spark and CW Source $OPD_{rms}$ (Empty Tunnel) . . . . .	56
4.8	A Comparison of the FS-LIB Spark and CW Source $OPD_{rms}$ (Blunt Body Present) . . . . .	56
4.9	A Comparison of the FS-LIB Spark and CW Source $OPD_{rms}$ (Extended Runtime) . . . . .	58
4.10	The dominant Zernike modes for the CW Laser and FS-LIB Spark Wavefronts (Tip/Tilt Removed) . . . . .	59
4.11	The most energetic POD mode for the FS-LIB Spark Wavefronts . . . . .	61
4.12	The CW Laser and FS-LIB Spark Source $OPD_{rms}$ compared to the Notre Dame Model . . . . .	62

## Chapter 1: Introduction

### 1.1 Motivation

Optical sensors on board a flight vehicle often have to look through a number of flow features, such as shock waves, turbulence, and shear layers. These flow features can affect a sensor's ability to correctly image their targets, to the point where the information collected is severely degraded from an optimal, "flow-off" state. The field of study surrounding the relationship between flow effects and sensor performance is known as "aero-optics" and has become essential for a range of applications from sensor and vehicle test and evaluation to the design of adaptive optics to combat image degradation[1]. An illustration of these effects is shown in Figure 1.1. The original motivation for the study of aero-optic effects stemming from fast-changing flow features came about during the 1970s and 1980s, when the development of airborne, turret-mounted high-energy lasers necessitated the understanding of how the turbulence around the turret would affect the far-field performance of the beam[1]. Ground-based turrets and telescopes typically only have to contend with optical distortions due to large-scale, low-frequency density changes in the atmosphere which can be corrected for using adaptive optics[2]. The turbulence over a flight vehicle, however, is much more chaotic, so the use of adaptive optics is not possible. Therefore being able to quantify the optical distortions so a vehicle can be designed to minimize them is critical[2]. This problem has carried over more recently to sensor

windows on high-speed vehicles, where shock waves, shock wave-boundary layer interaction, and active cooling jets create further aberrations that a sensor must look through.

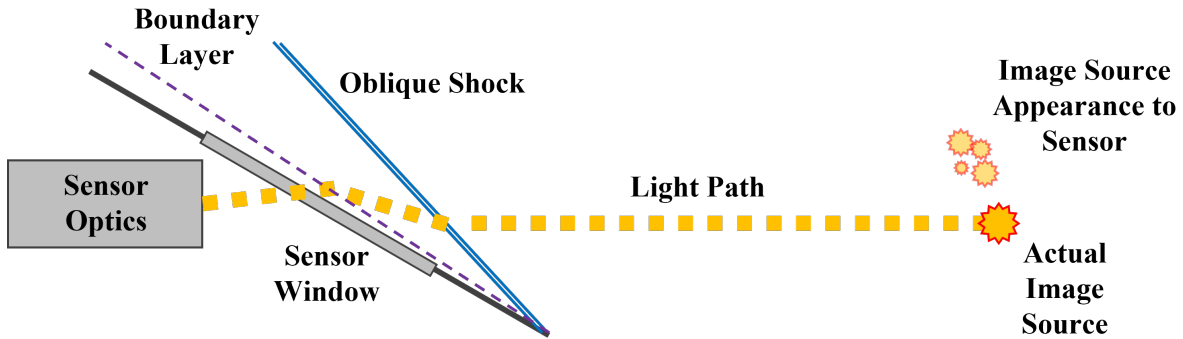


Figure 1.1: An Illustration of How Flow Features Can Alter a Sensor’s View of an Object

The importance of understanding how these flow features degrade an optical sensor’s performance has driven the study of aero-optic effects in test and evaluation environments. There are several parameters used to quantify the quality of an image viewed in the far-field by an optical sensor. These can be related back to the change in the optical path length (OPL) of the incoming light. The OPL depends on the index of refraction of the medium through which the light passes. This in turn depends on the density of the medium in fluids via the Gladstone-Dale constant[1]. The analytical relationship for this is shown below:

$$n = 1 + K_{GD}\rho \tag{1.1}$$

Spatial variations in density over the surface of a sensor’s aperture can change the local OPL of the incoming light. Nominally, a source viewed in the far field should appear to emit light with a planar wavefront. This is often used as a “reference” wavefront shape for aero-optic measurements. Flow features such as shock waves and turbulence create deviations in this planar wavefront due to pronounced changes in density. These deviations in the optical path from the

nominal wavefront are known as optical path differences (OPD) given by[2]:

$$OPD(x, y, t) = OPL(x, y, t) - \langle OPL(x, y, t) \rangle \quad (1.2)$$

Here, the variables  $x$  and  $y$  represent spatial locations on a sensor's aperture, and the term in brackets denotes the spatial average. OPD is what is often measured (either directly or indirectly) in modern aero-optics experiments[2]. Figure 1.2 illustrates the change in wavefront shape due to flow features. There are some theoretical relationships that exist for the OPD due to changes in flow properties[3], but quantifying the aero-optic distortions experimentally is still desirable. Ground testing facilities such as wind tunnels are one tool for collecting this aero-optic data for a new vehicle design. Ground test facilities install sensing optics designed to collect data on how the wavefront of incoming light has been distorted into a model of the vehicle of interest. In order for aero-optic data to be collected in ground testing, some sort of artificial optical target must be provided for the sensor to view that simulates an object in the sensor's far-field view. Historically, the most common way of providing light for the sensor to image is through the use of a collimated laser source which is projected through the flow field toward the sensor, since a collimated laser has a nominally flat initial wavefront and is therefore analogous to a far-field object.

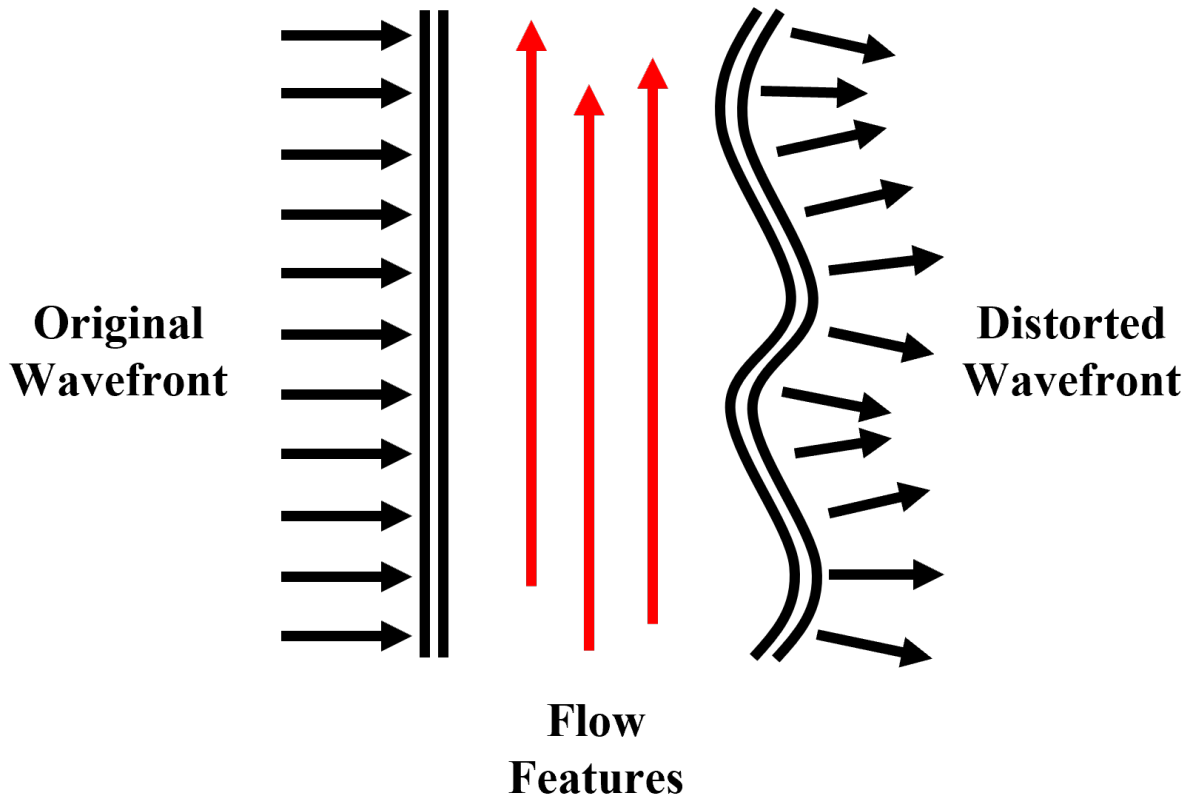


Figure 1.2: An Illustration of the Change in Wavefront Shape Due to Flow Features

One drawback to collecting aero-optic data in this way is that the range of available sensor viewing angles relative to a sensor's mounted location in a test article is limited, usually by the hardware used to introduce the collimated beam into the flow. In some cases, the location of a sensor in a test article means a collimated beam cannot reach it. For example, mounting hardware to steer a laser beam directly in front of a test article in a wind tunnel is intrusive and would create additional flow disturbances that would corrupt the desired measurement. An illustration of this is shown in Figure 1.3. Therefore, for these test conditions, a non-intrusive way of introducing light into the sensor's field of view is desirable. Laser-Induced Breakdown (LIB) sparks have been tested previously as one solution for this problem. LIB sparks offer the ability to place an optical source nearly anywhere in the flow-field, and can be created fairly

easily with the use of a nanosecond pulsed laser. However, the breakdown triggered by a typical nanosecond laser is violent, and the resulting LIB spark tends to move around significantly pulse-to-pulse[4]. In addition, the breakdown process itself also creates small disturbances in the flow that produce further unwanted aero-optical distortions outside of those produced on the test article. Furthermore, the pulse rate of most nanosecond lasers is on the order of tens of Hz, meaning that the frame rate at which data is collected is limited by how fast the laser creating the LIB spark can pulse. Studies have been conducted demonstrating the LIB spark in a variety of flow conditions to date, and these pluses and minuses have been well-characterized. However, ways of minimizing the impact of LIB sparks on aero-optic data collection is still a work in progress. In particular, there is interest in finding ways to minimize the movement pulse-to-pulse of the spark, so less work has to be done to remove the effects of this on the aero-optic wavefront data.

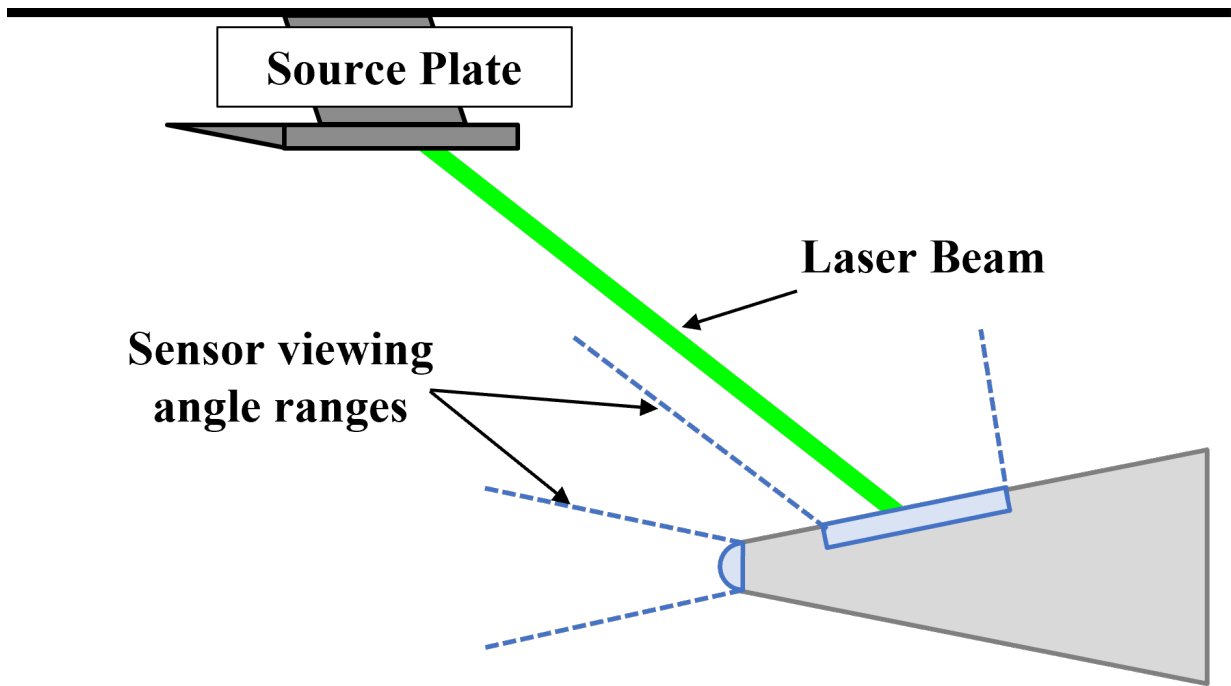


Figure 1.3: An Illustration of a Test Article in a Wind Tunnel with Two Viewing Angles Shown Along with a Collimated Laser Source for Illumination

Recently, a new form of laser-induced breakdown triggered by a femtosecond-pulse length laser has gathered interest for a variety of applications, notably spectrometry and combustion diagnostics[5]. The femtosecond laser-induced breakdown (FS-LIB) process is much less violent and produces a much more consistent emission pulse-to-pulse than its nanosecond counterpart thanks to the much shorter pulse length of the fs-laser. The increased shot-to-shot consistency and smaller disturbances created by the FS-LIB process make it an appealing alternative to “conventional” LIB for use as an aero-optic source. However, to date, no attempts at using an FS-LIB spark as an aero-optic source have been made.

## 1.2 Prior Research

### 1.2.1 Current and Previous Aero-Optics Testing

The first studies of the relationship between density fluctuations in a fluid and the index of refraction of the fluid date back to work done by Liepmann, who was trying to determine the sensitivity of refraction-based optical techniques such as Schlieren imagery. As time progressed, several other applications emerged for aero-optic data, including the development of adaptive optics for ground-based observatories and quantifying the dispersion of a laser beam projected out into a moving flowfield[6]. More recently, the need to understand how aero-optic distortions affect the performance of directed energy weapons and infrared sensors has driven the need for effective aero-optics ground testing. To this end, facilities that can study aero-optic effects in a variety of flow regimes from subsonic to hypersonic have come online[7]. Additionally, starting in the 1980s and 1990s, the development of computational fluid dynamics software to model turbulent structures meant that aero-optic distortions could be studied in a simulated environment

as well as an experimental one. Initially, these efforts were limited by available computing power[8], but now they have become more commonplace. The combined use of simulation and ground testing provides an extensive suite of tools to conduct analysis of the aero-optic distortions created by the flow moving around an object of interest.

One of the primary sources of aero-optic distortions is a turbulent boundary layer. Turbulence can form on flight vehicles moving at almost any speed, and therefore understanding how the turbulent boundary layer influences the  $OPD_{rms}$  of an incoming or outgoing beam has been studied extensively. Currently, there are theoretical models that have been developed for a turbulent boundary layer over a flat plate or a flat wind tunnel wall. One such model that has been tested at a variety of conditions is the Notre Dame model, first proposed by Gordeyev[9]. This model was initially developed in a subsonic and transonic compressible flow environment and has subsequently been tested in supersonic[10] and hypersonic[11] conditions. Currently, it accurately models the optical distortions created by a turbulent boundary layer up to Mach 5, and work is ongoing to increase the range of applicable conditions for which it can be used. The model is primarily dependent on the freestream Mach number and boundary layer information, as given in the following equation:

$$OPD_{rms} = F(M)K_{GD}\rho_{inf}M^2\delta\sqrt{C_f} \quad (1.3)$$

Here  $k$  is the Gladstone-Dale constant,  $\rho_{inf}$  is the freestream density,  $\delta$  is the boundary layer thickness, and  $C_f$  is the local skin friction coefficient. This form of the equation also assumes the light is propagating normal to the direction of the flow where the boundary layer is present and passes "top-down" through the boundary layer. The function  $F(M)$  is dependent only on

freestream Mach number, and curves of this function for a variety of freestream mach numbers can be found in[11], spanning the tested Mach number in this work. These curves have been generated based on empirical relationships, and no exact formula that is accurate over the range of applicable Mach numbers currently exists. The skin friction coefficient used in this model is the von-Karman-Schoenherr correlation with a compressibility correction applied[12].

The primary tool used to collect data on aero-optic distortions in the present day is the wavefront sensor. One of the most commonly-used wavefront sensors for visible wavelength measurements, such as those done in conjunction with a laser-induced breakdown (LIB) spark, is the Shack-Hartmann sensor[13]. The advantage of the Shack-Hartmann sensor is that it can re-create a full two-dimensional map of the OPD over its aperture, unlike other probes which only work in one dimension. This allows for the construction of the spatially-averaged  $OPD_{rms}$  of each wavefront. The Shack-Hartmann sensor does not measure the OPD directly, but rather measures the change in local propagation direction of the incoming light. A Shack-Hartmann sensor consists of a microlens array mounted in front of some sort of detector such that the focal points of the microlenses are coincident with the detector face. When an incoming optical wavefront passes through the microlens array, each section of the wavefront is focused onto a different region of the detector, resulting in a grid of points. Nominally, with a planar incoming wavefront, these points should form an evenly-spaced grid, and when the wavefront is distorted these points will be displaced from their nominal locations. A graphic illustrating this is shown in Figure 1.4.

Knowledge of these displacements as well as some of the specifications of the microlens array allow for the calculation of the OPD in each region, and this information can then be spatially averaged to calculate the  $OPD_{rms}$  as mentioned previously. This process will be discussed

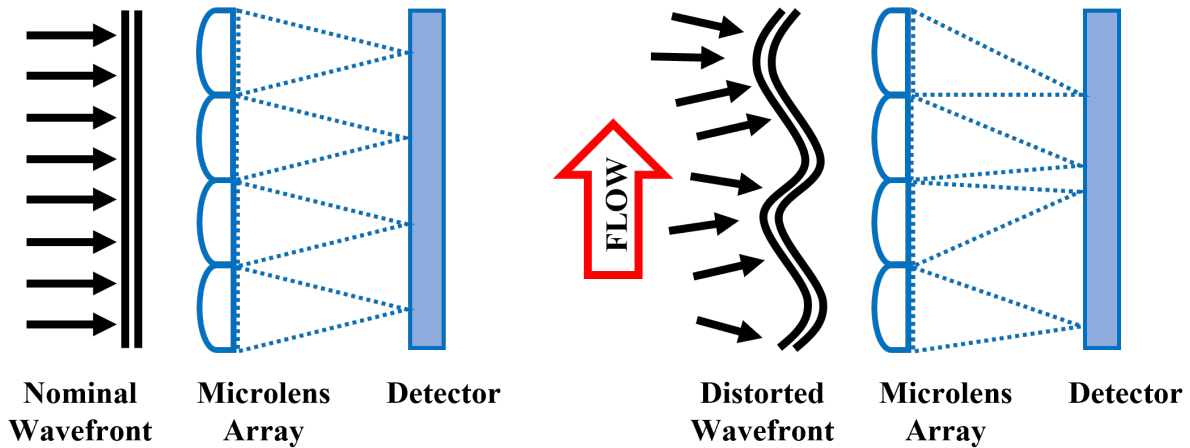


Figure 1.4: Illustration of the Shack-Hartmann Sensor Operation

in more detail in a subsequent section. The simple design of this sensor, consisting of only two major components, means it is also fairly straightforward to set up and use, and the performance of the sensor can be controlled by the combination of microlens array and detector used to comprise the sensor.

### 1.2.2 Wavefront Data Processing

The typical process for converting raw images collected with a Shack-Hartmann wavefront sensor into the wavefront error is as follows. First, the raw images are divided up into subapertures, each nominally centered around one lens image from the microlens array. Then, the centroid of the lens image in each subaperture is located. This location is then referenced to a nominal position, either defined as the center of the subaperture or the centroid location of the average tare image from the dataset. Then, the slopes of the lines drawn from the "delta" centroid locations back to the microlens array are calculated. These slopes generated from this comparison are converted into a wavefront "height" map, which is used to reconstruct the shape of the wavefront imaged.

The de-facto approach for converting lens array slopes into wavefront data was developed in the 1980s by Southwell[14], and has been modified and adapted for a variety of uses and remains an accepted standard for wavefront data processing. Southwell’s algorithm is based around solving a system of equations relating the displacement of each image centroid produced by the microlens array to the wavefront height at that lens. This relationship for a microlens in location (j,k) on the array is given in:

$$\phi^{j,k} = \frac{1}{4}(\phi^{j-1,k} + \phi^{j+1,k} + \phi^{j,k-1} + \phi^{j,k+1}) + \frac{h}{8}(S_x^{j-1,k} - S_x^{j+1,k} + S_y^{j,k-1} - S_y^{j,k+1}) \quad (1.4)$$

Here,  $\phi$  represents the change in wavefront optical path at each microlens’s region of interest, and S represents the slope at each location that was calculated previously. Note that slopes in both axes are typically calculated (given by the subscripts x and y) but only one slope is used depending on the location of the neighboring microlens relative to the one where the height calculation is being made. In order to solve this system for the wavefront height at the point of interest, several methods have been developed, including both iterative and direct approaches. Southwell made use of successive over-relaxation (SOR) in his original paper. Other iterative methods, such as Gauss-Seidel, have been applied to the Southwell method[15], but Southwell states that SOR provides the fastest convergence time while still maintaining accuracy of the iterative methods. Direct methods, such as singular value decomposition, have become popular more recently and offer advantages like the ability to pre-compute matrices to make the overall computation faster[16]. Modifications have also been made to the Southwell equations themselves, such as those done by Pathak[15] and Phuc[17] where the microlenses diagonal to

the one of interest are included in the slope calculations as well as those in the cardinal positions. This method has shown a marginal increase in accuracy but requires more computational time.

In order to calculate the displacements of the lens images, their locations must first be accurately determined. This is typically done by some sort of centroiding process. Several methods have been examined in literature. Two effective methods are the Gaussian centroid approach[18] and the first-order centroid approach with a threshold and a gamma correction applied[19]. The modified first-order approach offers the benefit of reduced computational time compared to the Gaussian approach, but the latter is not dependent on user-selectable parameters such as thresholds and gamma levels. Therefore it is more consistent across multiple sets of data.

### 1.2.3 Aero-Optic Guide Stars

Aero-optic guide stars, or beacons, offer the ability to place the illumination source virtually anywhere in space, meaning they can be used in environments or configurations where a "conventional" collimated laser source would not be practical or even possible. A common way to create a guide star is through the use of laser-induced breakdown (LIB) forming a small region of plasma at the focus of a pulsed laser beam. The term "breakdown" is loosely tied to the formation of enough ions in a region of a substance to scatter the laser beam, which then leads to a rapid formation of plasma throughout the duration of the laser pulse in the region where the laser beam intensity is high enough to have stimulated the ionization. This plasma is incredibly hot, and emits radiation in the visible spectrum as well other non-visible radiation[20]. This process is also often associated with a loud popping or cracking noise.

Several works have been published documenting the use of laser-induced breakdown (LIB)

sparks as aero-optic light sources to date. Early work in evaluating the characteristics of LIB sparks in an aero-optic context came from the Naval Surface Warfare Center as published by Neal et. al. in the late 1990s[21]. This work studied the spark in both a static vacuum cell as well as in a hypersonic flowfield, and most of the data they collected were at a low ambient pressure. To generate the spark, Neal et. al. made use of ND-YAG and ND-YLF nanosecond lasers, commenting that these were the only readily available lasers capable of sufficient intensity to produce breakdown at the time. The results collected in this work showed that the majority of the spark's motion pulse-to-pulse was in the direction of beam propagation, and that this pulse-to-pulse motion introduced additional errors into the aero-optic data. Additionally, they noted that changes in the spark's dimensions could lead to an apparent change in the spark's centroid location, which was shown to result in more errors in the data. They concluded that the reproducibility of the LIB spark needed to be improved in order for it to be a more effective source for aero-optic measurements.

More recently, most of the work characterizing the performance of a LIB spark has come from the Notre Dame Aero-Optics group. Rennie et.al. first characterized the behavior of the spark itself and noted that the finite size of the spark and its movement pulse-to-pulse were the primary sources of noise in aero-optic measurements[22]. After this, aero-optic data were successfully collected using a LIB spark as a source illuminating a compressible shear layer[23], in still air[4] and in a supersonic boundary layer[24]. The LIB spark created for these experiments was produced using a frequency-tripled Nd:YAG laser and focused using several focal length lenses to determine their effect on spark shape and movement. The result was generally a spark anywhere from 2-4mm in its longest dimension depending on the pulse energy of the laser and the focal length of the focusing lens. All of this data was collected with the wavefront sensor oriented

at a fairly low angle relative to the direction of beam propagation. Later work by Nguyen et. al. revisited the LIB spark research studying a variety of angles between the wavefront sensor and the beam propagation direction, all the way up to having the spark viewed orthogonally by the wavefront sensor[25].

When studied in still air, the LIB spark was shown to move and change shape significantly pulse-to-pulse. The changes in shape and position were also shown to create additional distortions in the wavefronts measured even with no flow present in front of the wavefront sensor. These distortions were broken down through the use of Zernike polynomials into a few dominant modes, primarily defocus, astigmatism, and coma[25]. These modes are not present in turbulent boundary layers, and as such could be removed from the wavefront data. After the removal of these low-order modes, the LIB spark provided similar levels of data quality to the CW source when studying turbulent boundary layers. In the earlier works by Rennie et. al. the dominant Zernike mode observed in the spark wavefronts was defocus. This corresponds to the fact that the spark was viewed at a shallow angle relative to the direction of propagation of the beam creating it. Therefore, most of its movement was either toward or away from the wavefront sensor[4][24]. Further work in this area by Nguyen et.al.[25] showed that, when viewed at steeper angles relative to the beam path, the movement of the spark manifested itself more in the higher-order Zernike modes. Additionally, Proper Orthogonal Decomposition (POD) was used to study the errors introduced by the spark, since the higher-order Zernike modes did not appear to accurately represent the behavior of the spark in the wavefront data since they appeared to be coupled together. All of these works stated that, while the LIB spark could be used to collect aero-optic wavefront data, the movement of the spark pulse-to-pulse still was challenging to fully characterize, and therefore minimizing the spark's movement would be beneficial to future work.

The works published by Rennie et.al. also demonstrated the need to select the appropriate optics for collimating the light produced by the LIB spark so that it could be passed through a wavefront sensor. Unlike a traditional collimated source, a LIB spark requires a collimating lens placed in front of the wavefront sensor for the latter to focus the incoming light through the microlenses onto the detector. The focal length of this lens has a lower bound. Below this bound, the apparent movement of the spark due to either flow features or the actual spark itself can cause the spark's "image" on the detector of the wavefront sensor to move beyond the subregions on the detector for each microlens. This results in the centroid position of the spark's image no longer being calculable and the measurement taken with the wavefront sensor invalid[4]. Another factor to consider is the effect of anisoplanatism. Anisoplanatism refers to the changing in apparent size of a disruptive flow feature in the view of a wavefront sensor due to the light it is illuminated by not being collimated. Since a spark is an approximation of a point source, the light it emits is expanding, so the beam passing through a flow feature of finite thickness expands in diameter slightly as it travels through the flow feature. This will change the amount of wavefront distortion the flow feature will appear to create as seen by the wavefront sensor. Experimental work has found that, if the ratio of the distances to the viewing aperture of the beacon and the aero-optic disturbance is great enough, then these effects do not contribute significantly to the overall aero-optic measurement error[26].

#### 1.2.4 FS-LIB

Compared to "conventional" laser-induced breakdown typically generated through the use of a nanosecond laser, femtosecond laser-induced breakdown (FS-LIB) is a newer technique that

has been rapidly gaining interest in a variety of fields. The reason for the less prominent use of FS-LIB is due to the demands of creating a femtosecond pulse with sufficient intensity to produce breakdown. Modern ultrafast laser systems making use of chirped-pulse amplification are most commonly used today to generate FS-LIB[27]. These laser systems consist of many parts, often including a ND:YAG or ND:YLF laser similar to those used for conventional LIB as a seed laser. Additionally, femtosecond laser pulses also are subject to a phenomenon known as filamentation, which is a manifestation of the balance between the self-focusing of the femtosecond laser beam and de-focusing effects of the plasma in the breakdown region. These filaments are also formed when a femtosecond laser pulse is focused to create breakdown and can be observed along the beam path near the breakdown region[28].

The ultrashort pulse length of a femtosecond laser means that breakdown created by focusing the beam does not undergo the same avalanche ionization process seen in nanosecond laser-induced breakdown. Avalanche ionization occurs where electrons stripped from the target gas are further energized by more photons from the emitted laser pulse, and eventually have enough energy to ionize more gas through collisions. This results in additional plasma formation beyond that from the initial laser pulse itself[27]. In air, this process requires a minimum timescale of about 350fs, so a beam with pulse duration shorter than this will not trigger the avalanche ionization process[27]. Therefore, the energy dissipation is much more predictable, and the plasma region created by the femtosecond pulse is more regular[29]. This has benefits in a variety of industries from micromachining to spectroscopy[30]. In particular, the field of combustion diagnostics has made use of FS-LIB to study the species present in a reaction[31] where the shorter pulse length and more stable resultant plasma formation allow for more accurate diagnostics. Additionally, FS-LIB has found success in combustion measurements in high-pressure environments

where nanosecond LIB has previously struggled[32]. However, unlike nanosecond LIB, FS-LIB has not yet been used to produce illumination sources for aero-optic applications. The same benefits that have made it a popular choice in other fields of study should make it an attractive option for an aero-optic light source.

### 1.3 Objectives

The primary objective of this thesis is to evaluate the viability of the FS-LIB spark as an aero-optic light source. The FS-LIB spark will be studied directly in order to determine what, if any, additional changes to the wavefront it introduces when using it to illuminate the flow. The FS-LIB spark will also be compared to a collimated source in order to determine if these additional changes to the wavefront shape can be removed effectively and the aero-optic wavefront distortions from the flow can be recovered. To accomplish this, a Shack-Hartmann wavefront sensor (WFS) will be used to make measurements of the turbulent boundary layers that form on the walls of a supersonic wind tunnel. The latter will provide a "canonical" set of aero-optic features to examine that can be compared between sources and also to existing theoretical models.

### 1.4 Approach

The first steps in validating the use of the FS-LIB spark are to determine how stable it is pulse-to-pulse, and analyzing the how much additional wavefront error is introduced by pulse-to-pulse movement or shape change. This will be done both through directly imaging the spark and by collecting wind-off wavefront images. Comparing the variations in the shape of the spark

and its centroid location to those reported previously for a "conventional" nanosecond LIB spark will indicate if the femtosecond breakdown process actually produces a more stable aero-optic source. If this is achieved, then there will be less wavefront error present in the data that would need to be removed in order to study the flow features of interest. The wavefront error will be quantified using techniques similar to those implemented for studying nanosecond LIB sparks in literature, including various types of modal analysis as explained previously.

Next, the FS-LIB spark will be used to measure wind-on distortions created by the turbulent boundary layers that form on the walls of supersonic wind tunnel. The aero-optic distortions created by a turbulent boundary layer have been well-characterized using other sources for a variety of flow speeds and therefore serve as a "canonical" distortion for assessing the effectiveness of the FS-LIB source. The wavefront error produced by the turbulent boundary layers will also be imaged with a continuous wave (CW) collimated laser source, which is an established illumination source for collecting aero-optic data. This will serve as a baseline for the wavefront data FS-LIB spark along with models reported on previously in literature. In addition to the M3T wall boundary layers themselves, the turbulence created behind a blunt body will be imaged to provide a second set of data points to compare the two sources used.

## Chapter 2: Methodology

### 2.1 Experimental Setup

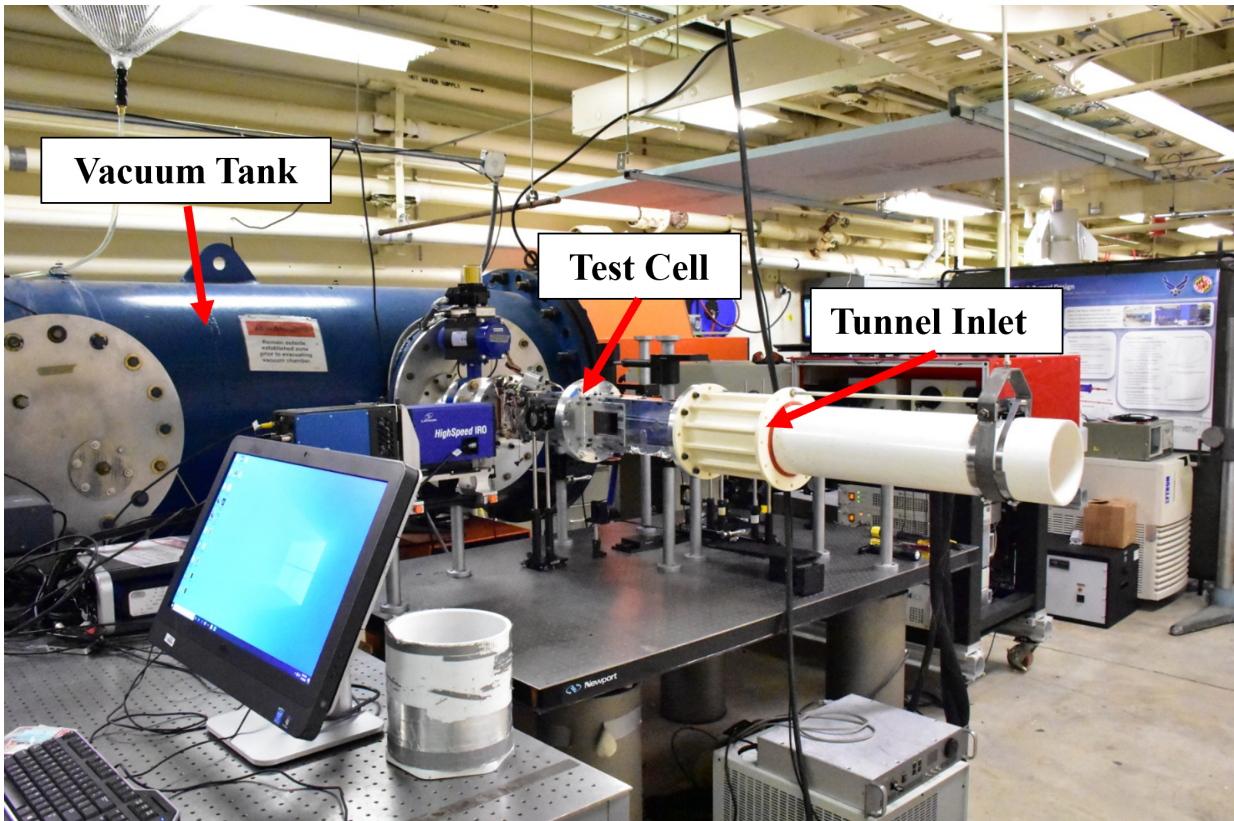


Figure 2.1: The Tunnel 9 Aero Cal Lab and Mach 3 Tunnel (M3T)

The facility used to produce flow to measure Aero-Optic phenomena is the Tunnel 9 Aero Cal Lab Mach 3 tunnel, henceforth referred to as the M3T. An image of the M3T with some features labeled is shown in Figure 2.1. The M3T is a miniature indraft supersonic wind tunnel

using ambient air at atmospheric conditions as a supply gas, and a large vacuum chamber as a low-pressure reservoir. The M3T nominally operates at a Mach number of 2.8 with a freestream Reynolds number of  $8.6e6/m$ . The test cell is approximately 2.5 inches square and consists of three window stations. Provisions to mount static pressure taps exist in various locations in the test cell, and these allow for monitoring of the freestream pressure during a run. In turn, this information can be used along with knowledge of the inlet conditions (which are ambient room temperature and pressure) in order to calculate various non-dimensional parameters related to the M3T's performance, such as the Mach number and Reynolds number. In order to estimate the magnitude of the aero-optic distortions generated in the M3T, the boundary layer on the tunnel side walls must be characterized. In addition to the static pressure taps, the M3T can optionally be run with an insert containing a small Pitot rake with twelve pressure taps. A series of calibration runs were collected prior to the main aero-optic data collection using this Pitot rake rake to assess the boundary layer thickness. The data presented here was collected in the second window station, which has an approximate sidewall boundary layer thickness of 12mm. This location is indicated in the close-up of the M3T test cell shown in Figure 2.2. Some general flow properties of the M3T are shown in Table 2.1. The side walls of the second window station were the region of the flow illuminated by the sources used in this work to collect aero-optic data, so the values in the table below reflect the freestream properties at this location.

Table 2.1: A Summary of M3T Flow Properties

$P_{inf}$ (torr)	$T_{inf}$ (K)	$\rho_{inf}$ (kg/m <sup>3</sup> )	$M_{inf}$	$U_{inf}$ (m/s)	Re/m	$\delta$ (mm)	$C_f$
28.7	115.4	0.1	2.8	598.6	$8.6e6$	12	$1.8e-3$

There were two different flowfields used to collect wavefront data to evaluate the performance of the FS-LIB spark. The first flowfield consisted of only the tunnel wall boundary layers. Since

models exist of the aero-optic distortions created by a flat plate turbulent boundary layer, this configuration allows for the comparison of the two illumination sources to the existing models as well as to each other. The second flowfield added the wake behind a sphere approximately 12mm in diameter (henceforth referred to as the blunt body) installed on a sting mounted ahead of the measurement location in the M3T test section. This provides additional aero-optic "signal" to measure since the wavefront sensor is now collecting data on the turbulent wake from the blunt body as well as the two tunnel wall boundary layers. The blunt body also caused unstart to occur in the tunnel earlier than with an empty test section. The unstart process was also imaged to study the relative transient response of the two sources. Figure 2.2 shows the test section of the M3T with the blunt body installed. The tunnel flow moves from right to left in the orientation this image was taken in. The lens mounted in front of the second window station indicates where the flow was being imaged by the wavefront sensor.

The laser used to generate the FS-LIB source in this experiment is a Spectra-Physics Solstice Ace Ti:Sapphire system. This outputs an 800nm wavelength beam carrying approximately 6mJ of energy per pulse, with a pulse width of 100fs. The laser system was set up to pulse at a rate of 1kHz for all of the data collected. The output beam is expanded to approximately 50mm in diameter before being re-focused through a 150mm focal length lens, to produce a f/d ratio of 3:1. This keeps the region where the intensity threshold is high enough for breakdown small, so the resultant breakdown spark created more closely approximates a point source. The light emitted from the FS-LIB spark passes through the M3T such that the imaged region of the boundary layer farthest from the source is 20mm in diameter. A diagram of the beam path is shown in Figure 2.4. Due to the point source-like nature of the FS-LIB emission, the closer of the two boundary layers is captured in a smaller imaged region approximately 14mm in diameter. As such the overall

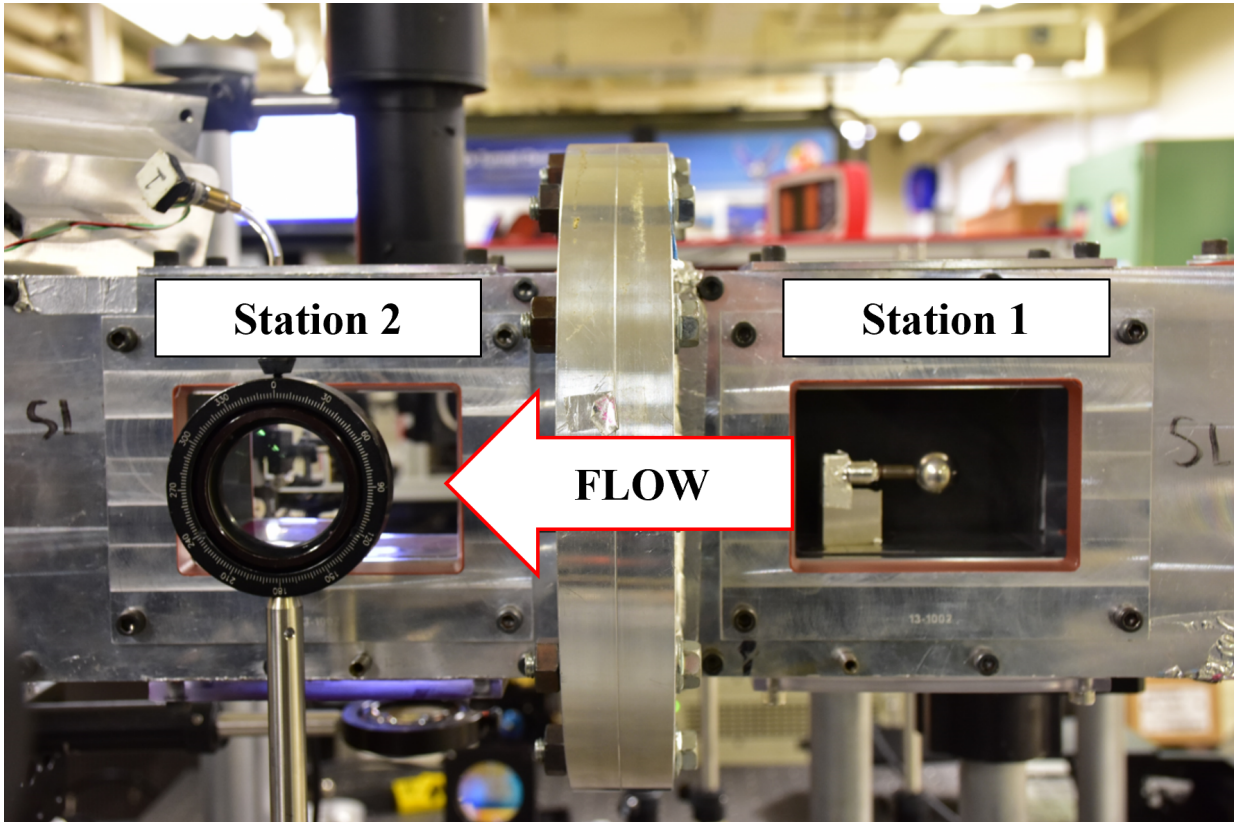


Figure 2.2: The Test Section of the M3T with the Blunt Body Installed

strength of the aero-optic distortions of the two boundary layers are similar but not identical. Therefore, this is an area where the results from the FS-LIB spark may differ slightly from the collimated source and aero-optic boundary layer theory. The reason for setting the FS-LIB spark outside of the M3T and imaging both boundary layers is due to the small cross-section of the test section. If the FS-LIB spark was placed inside the M3T's test section such that only one boundary layer was illuminated, the aperture size would be very small, and the resulting  $OPD_{rms}$  calculation would be difficult. After passing through the M3T, the light from the FS-LIB source is collimated by a 250mm focal length plano-convex lens before being passed to the wavefront sensor. The collimating lens is placed opposite the tunnel from the spark in order to replicate a larger-scale wind tunnel application, where this collimating lens would likely be inside the

test article just ahead of the wavefront sensor and downstream of the flow features distorting the incoming wavefront. Figure 2.3 shows the spark projected in space just outside the windows of the M3T.

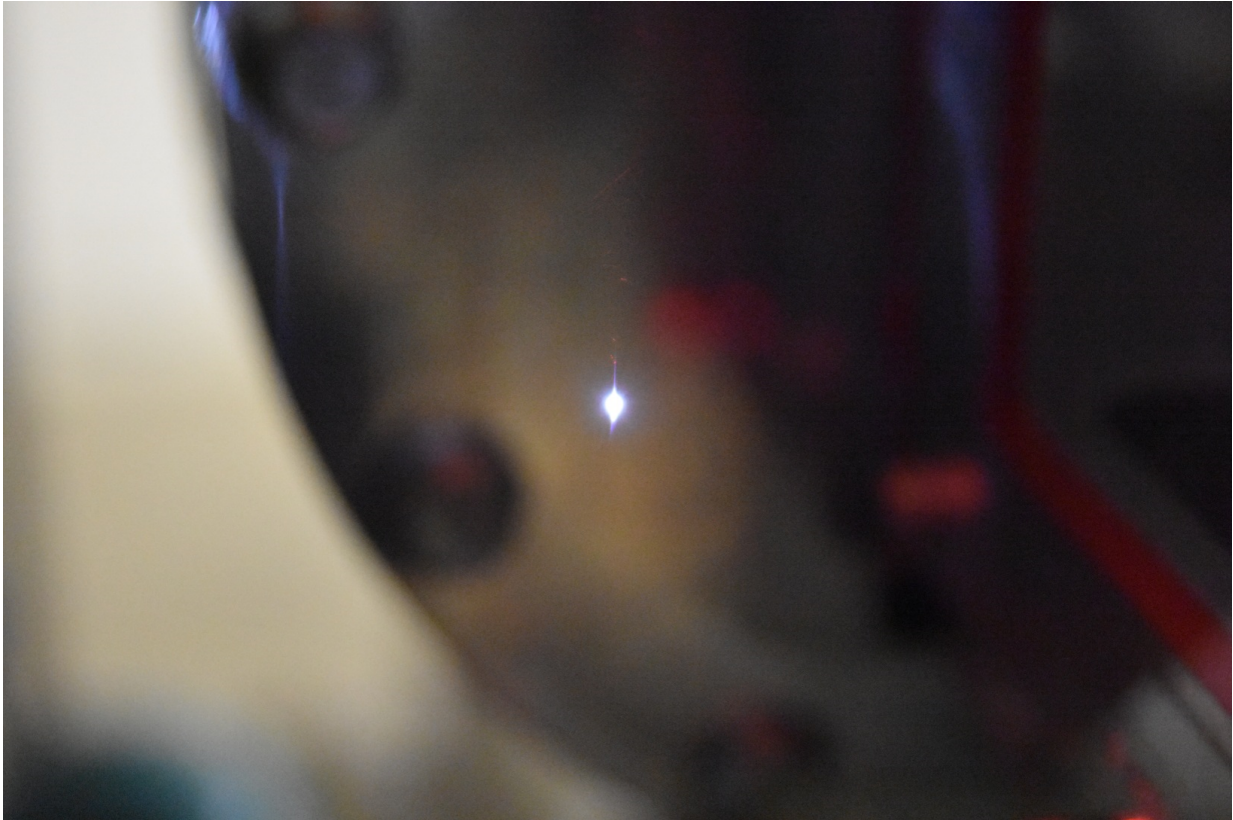


Figure 2.3: The FS-LIB Spark

A collimated beam is also generated for comparison to the FS-LIB spark. The light source is a Lightwave Model 212E diode laser producing a continuous wave 532nm beam. The beam is passed through a 60:1 objective lens to expand the beam to approximately 50mm in diameter then sent through a 20mm diameter aperture and re-collimated through a 200mm focal length lens. The beam path for the collimated source is shown in Figure 2.4. This combination of sending optics was selected to provide as close to an even intensity distribution as possible on the wavefront sensor. Since the FS-LIB source is placed such that the imaged region on the

far tunnel window is also 20mm in diameter, the collimated source will have the same ratio of aperture size to boundary layer feature size. However, unlike the FS-LIB source, the collimated source wavefront data will not be altered by the effects of having two different aperture sizes for the two tunnel wall boundary layers. After passing through the tunnel, the collimated beam is re-sized to 25mm in diameter via a telescope before entering the wavefront sensor. This is done because the light from the FS-LIB spark continues to expand after exiting the M3T and before being collected by the collimating lens. Therefore, the 20mm diameter beam on the M3T wall will grow to 25mm by the time it reaches the collimating lens. Re-sizing the collimated laser beam ensures the features will be the same as those imaged by the FS-LIB spark when they reach the wavefront sensor. While this does not provide a perfect comparison between the two sources, it makes the images produced by each appear as similar as possible on the wavefront sensor to minimize differences created by the experimental setup. A complete optical diagram is shown in Figure 2.4. Note that the two sources are shown here simultaneously for compactness. In reality, each source was used on its own for separate runs.

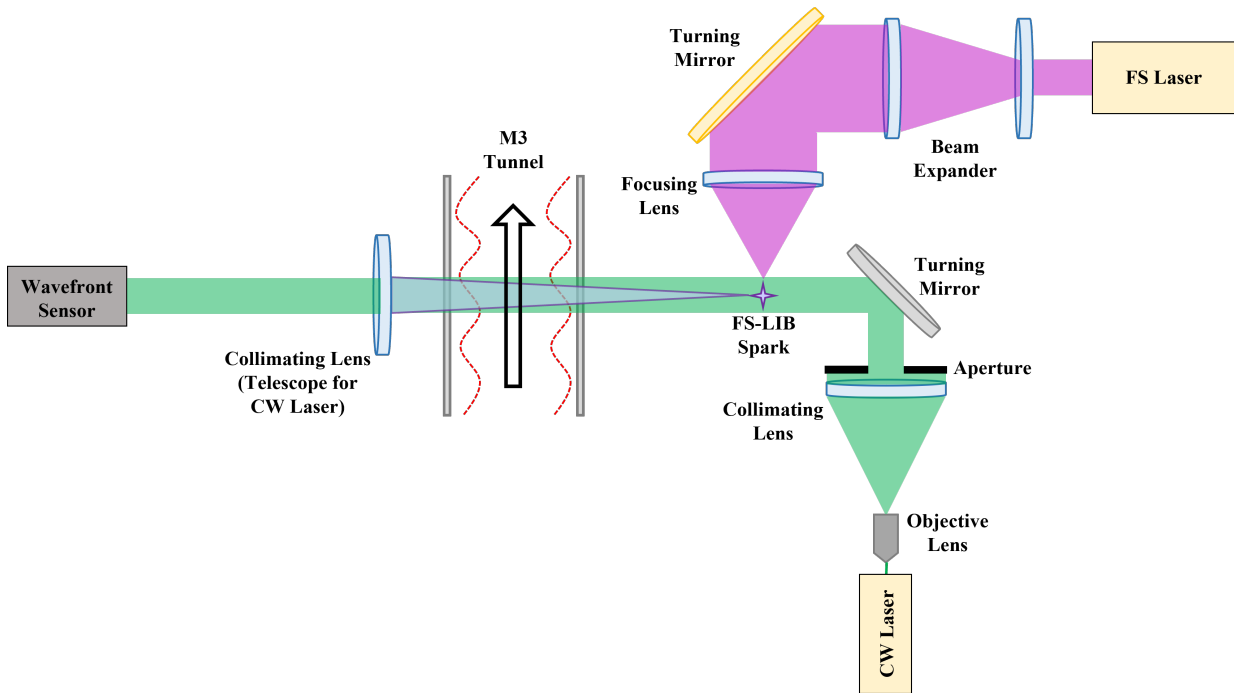


Figure 2.4: Optical Diagram Showing Both the Collimated Source and FS-LIB Spark Paths

A Shack-Hartmann wavefront sensor is used to collect raw focal spot displacement images of the illumination from the FS-LIB spark and the collimated laser source. The sensor consists of the illumination from the FS-LIB spark and the collimated laser source. The sensor consists of a Suss Microoptics microlens array containing 100x100 microlenses. Each microlens has a pitch of 500 $\mu$ m and a focal length of 44mm. The focal spots from the microlenses are imaged onto a LaVision High Speed IRO that is connected to a PCO Dimax HD camera. The intensifier is synced to the laser pulses through the use of a separate pulse generator, which reduced the rate of image collection to 100Hz. This was done for two reasons. First, the reduced image count allowed for faster data processing, and since the laser pulse rate of 1kHz was still not fast enough to capture time-resolved images of the flow structures, there was no loss in data fidelity. Second, the reduced frame rate allowed for an entire run of the M3T to be captured without running out of space on the PCO camera's buffer. As mentioned previously, this allowed for the collection of run data when the tunnel unstarts at the end of a run to observe the change in wavefront error

the unstart creates. The camera is set to have a  $6\mu\text{s}$  exposure and a  $9994\mu\text{s}$  delay to capture the output from the intensifier. The PCO camera has a ROI of  $1920 \times 1440$  pixels and a pixel size of  $11\mu\text{m}$ . The FS-LIB spark was also imaged directly through the use of an IDT Os9 high-speed camera in order to capture information on the change in the spark's shape and size pulse-to-pulse. The frame rate on the IDT camera was set to match the intensifier, and the delay set to match the PCO camera. Additionally, the same sync and trigger signals were used for both camera systems. This allowed the two cameras to run in-sync with one another, so the spark images and spark wavefronts could be related to one another during data processing and analysis. Images of the microlens array and the IDT camera are shown in 2.5.

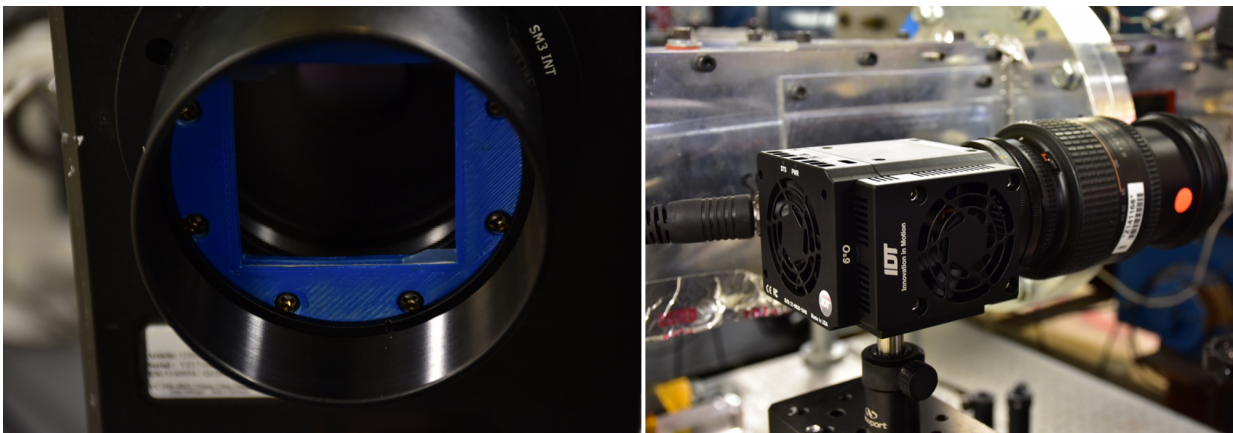


Figure 2.5: The Two Cameras Used to Collect Data on the Spark. On the Left is the Microlens Array Mounted in the Intensified Camera and on the Right is the IDT Camera with Zoom Lens

## 2.2 Run Matrix

In order to collect enough data to draw robust conclusions about the performance of the FS-LIB spark, several runs were completed using the M3T in each of the two aforementioned configurations. The test matrix for the data presented in this thesis is shown in Figure 2.6. Data were collected for five seconds during most of the tunnel runs, of which approximately three

seconds was steady "good flow" wind-on data and the rest captured the tunnel start-up behavior. Two runs were extended to capture tunnel un-start as well. Five runs were taken each with the FS-LIB spark and the CW laser as a source of the M3T with an empty test cell so that only the boundary layers would be observed. Additionally, six runs were taken with each source with the blunt body installed upstream of the measurement location. Data captured for five of these six runs was over the same time span as used for the empty tunnel runs, and the remaining run included the aforementioned un-start data. Data collected during all runs also included one hundred pre-trigger "wind-off" images. These were used by the data reduction code to remove additional aberrations created by the optics as will be discussed in the next section. A run matrix summarizing the runs used in this work is shown in Figure 2.6.

In addition to the runs shown in the matrix in this work, several calibration and shakedown runs were collected in order to test various aspects of the experimental setup. These included runs with different microlens arrays installed in the wavefront sensor, different receiving optics for both sources, and even runs where pure nitrogen was used as a supply gas instead of ambient air. In the end, it was found that varying these parameters did not have a significant impact on the quality of the data collected, which allowed for the selection of the experimental setup used for the main data collection campaign.

Run Number	Source	Lens Array Pitch (um)	Tunnel Config	Frame Rate (fps)	IDT Camera? (If FS)	Comments
FS_BB_01	FS-LIB	500	Blunt Body	100	YES	
FS_BB_02	FS-LIB	500	Blunt Body	100	YES	
FS_BB_03	FS-LIB	500	Blunt Body	100	YES	
FS_BB_04	FS-LIB	500	Blunt Body	100	YES	
FS_BB_05	FS-LIB	500	Blunt Body	100	YES	
FS_BB_06	FS-LIB	500	Blunt Body	100	YES	Extended run time to see tunnel shutdown
FS_CF_01	FS-LIB	500	Empty	100	YES	
FS_CF_02	FS-LIB	500	Empty	100	YES	
FS_CF_03	FS-LIB	500	Empty	100	YES	
FS_CF_04	FS-LIB	500	Empty	100	YES	
FS_CF_05	FS-LIB	500	Empty	100	YES	
CW_BB_01	CW Laser	500	Blunt Body	100		
CW_BB_02	CW Laser	500	Blunt Body	100		
CW_BB_03	CW Laser	500	Blunt Body	100		
CW_BB_04	CW Laser	500	Blunt Body	100		
CW_BB_05	CW Laser	500	Blunt Body	100		
CW_BB_06	CW Laser	500	Blunt Body	100		Extended run time to see tunnel shutdown
CW_CF_01	CW Laser	500	Empty	100		
CW_CF_02	CW Laser	500	Empty	100		
CW_CF_03	CW Laser	500	Empty	100		
CW_CF_04	CW Laser	500	Empty	100		
CW_CF_05	CW Laser	500	Empty	100		

Figure 2.6: The Run Matrix Showing all Runs Used for the Present Work

### 2.3 Data Collection Process

A typical data collection run proceeds as described here. First, the optical setup is configured to either take data with the collimated laser source or the FS-LIB spark source. This involves installing the required collimating optics for one of the two sources as described above in their respective sections. Then, the laser and all other electronic devices are powered on and the laser is allowed to warm up. While the laser is warming up the Cal Lab Mach 3 tunnel (M3T) is prepared for running. This involves powering up the pump for the vacuum tank and supplying the control valves with compressed air for operation. Once the M3T is configured to run and the laser is warmed up, a cap is placed on the end of the M3T nozzle. Then, a vacuum is pulled on the test cell with pressure measurements taken during the pulldown process. This is done to verify the response of the pressure tap installed in the test cell against three MKS Baratron pressure transducers, which have NIST-traceable calibrations. At this time, the vacuum tank is also pulled

down to a back-pressure of approximately 10 torr for running the tunnel. Once the pressure tap check is complete, the test cell is vented back up to atmosphere, the laser shutter is opened and the camera turned on briefly to double-check the quality of the raw microlens array images. The camera is then set to record, and the valve separating the M3T from the vacuum tank is opened. This valve remains open until a preset back-pressure in the vacuum tank is reached, which is typically set to 200 torr. This back-pressure was chosen because it allows the tunnel to run just until it un-starts due to no longer having a favorable pressure ratio, therefore giving maximum run time. A typical run length for the tunnel with nothing present in the test cell is on the order of ten seconds, with approximately seven seconds of steady "good flow" conditions. This is reduced to approximately five seconds of good flow with the blunt body installed in the tunnel, after which the tunnel unstarts. After the run is complete, the images and pressure tap data are saved, and the vacuum tank and test cell are vented to atmosphere once more.

## 2.4 Data Reduction Process

The first step of the data reduction process was to analyze the size and shape of the FS-LIB spark. The images of the spark collected by the IDT camera were brought into a MATLAB code that converted the raw images into binary images. This allowed for the calculation of the spark's width and height in pixels. To convert this to engineering units, images were taken of a target card and measured in MATLAB to determine the number of pixels per millimeter in the spark images. A mean image was generated from each set of images, and the RMS of the deviation from this mean image was calculated to determine the change in spark size pulse-to-pulse. Additionally, the centroid of the imaged spark area was calculated and the pulse-to-pulse deviation from the

mean of this centroid location was also calculated.

Next, the images collected by the Shack-Hartmann wavefront sensor were processed to generate wavefront maps. In order to convert the wavefront sensor images into actual wavefronts, a second MATLAB code was utilized. The raw wind-off images are first averaged to produce a mean wind-off image and the code calculates the approximate locations of each microlens in the mean image and generates subapertures for each microlens based upon these locations. Then, the centroids of each microlens are calculated using a first moment centroiding technique with a fourth-order gamma correction, as tested by Nightengale and Gordeyev[19]. The locations of the microlens spot centroids from each image are referenced to the center of each region to generate the spot displacements. The wavefront phase error is calculated using the Southwell method as described previously. The series of equations used in the Southwell method are placed into matrices and inverted directly using Matlab's built-in pseudo-inverse command. Since the matrix containing the sub-region information is the same for all images, it is calculated and inverted before each image is processed in order to speed up computation time.

Once the wavefronts are generated for each image, the code performs several post-processing steps to extract aspects of the spark's performance and compare it to the CW laser data. First, a mean tare image is generated and then subtracted from each run image in order to remove effects from the optics in the experimental setup. Then, the tip, tilt, and mean displacement of each wavefront is calculated, and a second set of tip/tilt removed wavefronts are produced. These tip/tilt removed wavefronts now nominally only contain the features produced by flow turbulence and any "noise" that is either a product of the experimental setup itself or the FS-LIB spark motion. The main data reduction process up to producing the tip/tilt removed wavefronts is shown in graphically in Figure 2.7. The tip and tilt for each wavefront is also plotted against

the FS-LIB spark's centroid displacement from the mean image in order to determine the level of correlation present between the two phenomena. Next, the  $OPD_{rms}$  of each tip/tilt-subtracted wavefront is calculated and plotted versus run time. Examples of these  $OPD_{rms}$  traces can be seen in Chapter 4 of this work. The average value of the  $OPD_{rms}$  is also calculated. Further analysis methods, such as a Zernike mode decomposition and POD, are performed after this step. The Zernike mode analysis is performed using the equations for the mode shapes identified in Noll's paper[33]. The POD analysis makes use of the "snapshot" method as described by Weiss[34]. Finally, the code outputs surface plots of the various wavefronts as well as GIFs of the wavefront over time. The code was validated through the use of "synthetic" lens array images generated in MATLAB that provided a grid of points with known locations. These synthetic images were designed to mimic simple, low-order optical aberrations that could easily be referenced to validate the performance of the data reduction code.

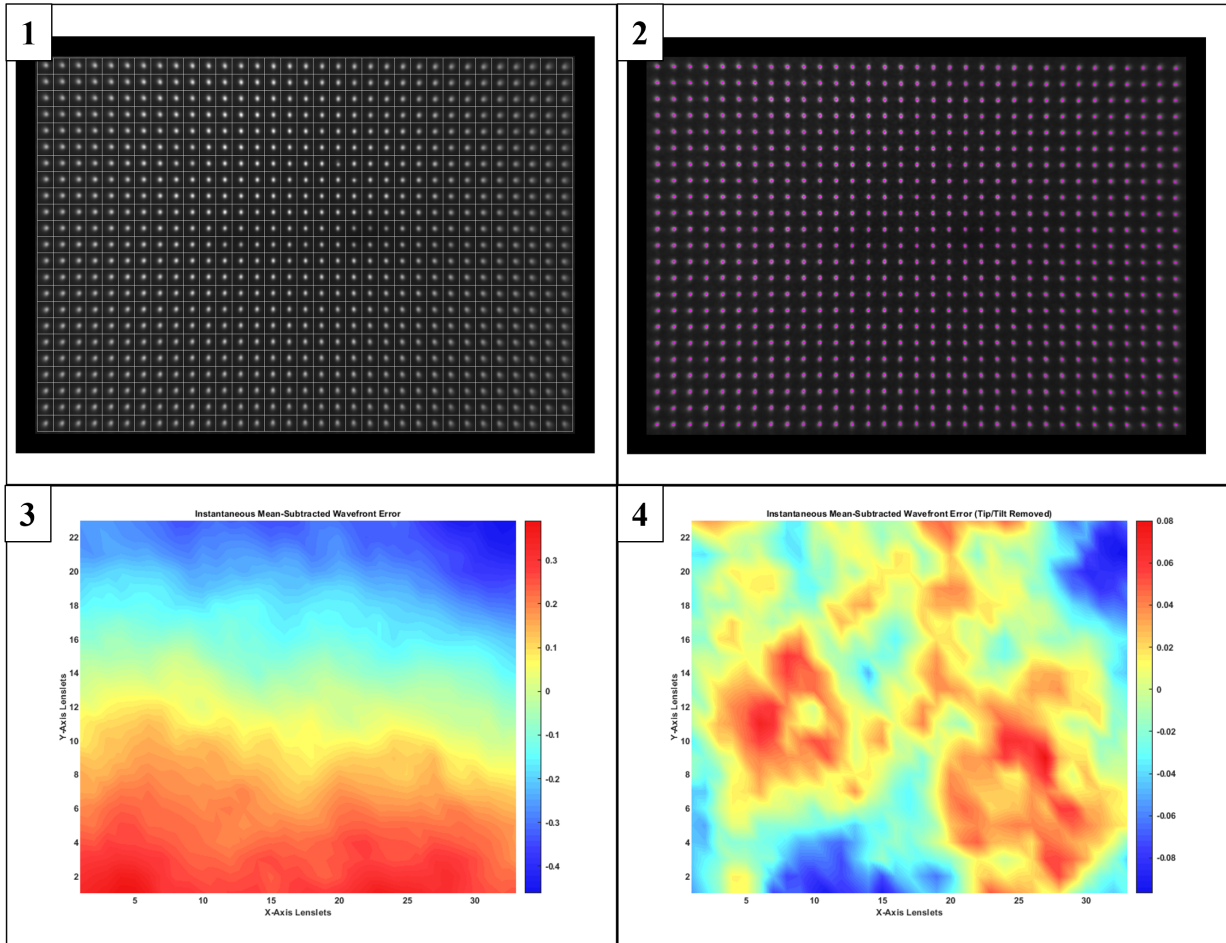


Figure 2.7: The Main Steps in the Wavefront Data Reduction Process. 1) Subaperture Generation, 2) Spot Centroid Location, 3) Mean-Subtracted Wavefront Generation, 4) Tip/Tilt Removal to Reveal Turbulent Features

In order to generate an estimate for the  $OPD_{rms}$  created by the tunnel wall boundary layers using existing theoretical models, the Pitot rake data was converted to a velocity profile through the use of the Rayleigh-Pitot formula as well as isentropic flow relations. The supply pressure was measured using the atmospheric reading from the MKS Baratron pressure transducers attached to the cal lab. The supply temperature was measured using a handheld thermometer with a type E thermocouple installed. These serve as total pressure measurements to calculate the tunnel freestream conditions with since the tunnel uses air at ambient pressure and temperature as a

supply gas. The velocity profile was then used to calculate the momentum thickness, which is used to generate the estimate for skin friction as outlined in Gordeyev et. al.[9]. The pitot rake data also provided a measurement of the overall boundary layer thickness, which is the remaining needed quantity to estimate the boundary layer's  $OPD_{rms}$ .

## 2.5 Uncertainty Analysis

All uncertainties presented in this work were estimated using the techniques laid out in ASME-PTC 19.1, Measurement and Uncertainty Analysis[35]. Systematic uncertainties were either pulled from datasheets for the hardware used in the experimental setup or estimated. All stochastic uncertainties were calculated using two standard deviations from the mean to provide a 95% confidence interval.

## Chapter 3: Results: Spark Analysis

### 3.1 FS-LIB Spark Size and Shape

Analysis of the size and shape of the FS-LIB spark using the data collected with the IDT camera is shown here. The majority of the images were collected of the spark projected into still air at atmospheric conditions, however a sweep of images at various pressures in a vacuum cell was also collected to observe the effects of decreasing the ambient pressure. At atmospheric conditions, the spark appeared on average to be just under 1mm long in the direction of beam propagation, and approximately 0.4mm normal to the direction of beam propagation. Unlike nanosecond LIB sparks, the shape of the FS-LIB spark is more uniform, with less of a prominent "tail" and more of a consistent oval shape. There is still a small amount of taper toward the direction of the beam source, however. An image of the spark as collected with the IDT camera at atmosphere is shown in Figure 3.1. The axes indicated on the image correspond to the directions normal to beam propagation (X-axis) and in the direction of beam propagation (Y-axis) and will be referenced in future plots to show directional dimension changes. Another interesting feature present in the FS-LIB spark that is not typically observed with a nanosecond LIB spark is the presence of two small "filaments" on either end of the spark itself. These seem to indicate that there is some filamentation characteristic of femtosecond laser beam propagation as mentioned previously present outside of the actual breakdown region. These small filaments are dim relative

to the oval-shaped breakdown region, and likely would not have much effect on a wavefront measurement collected using the FS-LIB spark.

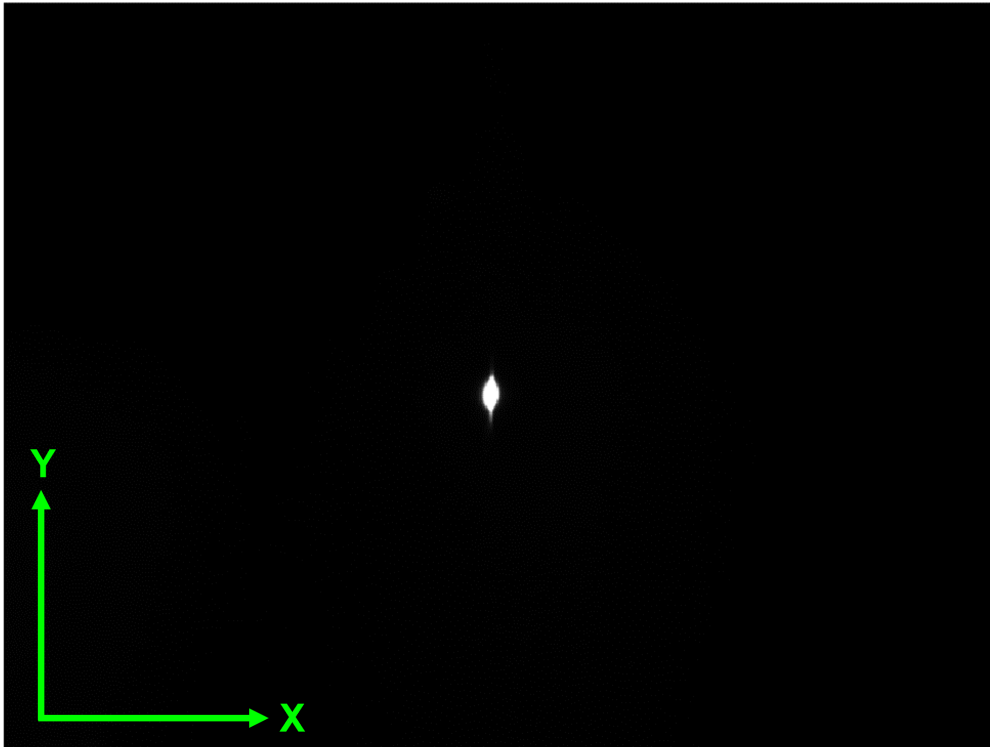


Figure 3.1: The FS-LIB Spark as Seen on the IDT Camera

The IDT camera collected images of the FS-LIB spark during each run where it was used to collect wavefront data. For each run, the complete set of images was averaged together to produce a mean spark image, which was used as the baseline from which all other measurements were obtained. One of the most important parameters to quantify in terms of pulse-to-pulse spark movement is the location of the spark's centroid in each image relative to the mean. Since the spark is essentially an approximation of a point source, the location of the centroid roughly corresponds to where the focal region on the wavefront sensor will be, and motion of the centroid

can then shift these focal regions, creating additional wavefront error. Therefore, minimizing the centroid movement is essential to good aero-optic data quality. For the FS-LIB spark, at atmospheric pressure, the norm of the motion of the centroid on average was approximately  $17\mu\text{m}$  with a standard deviation of approximately  $12\mu\text{m}$ . This is less than two percent of the total spark height. Furthermore, the camera setup produced images that had approximately 25 pixels per millimeter in the view used to image the spark, or put another way, each pixel is about 40 microns to a side. Therefore, the spark centroid displacement corresponds to less than half of a pixel on the image. To the naked eye, this motion is almost imperceptible. Figure 3.2 shows the norm of the displacement of the spark centroid as referenced to the mean image over the course of one run. Here the spread of the centroid deviation from the mean can be seen in more detail. Note that there appear to be a small number of images with a significantly larger centroid shift than the vast majority in the data presented. These more extreme shifts appeared to some extent in all of the run data collected. They were included in the calculation of the averages for each run since it is unclear if they are truly outliers or just the outer extreme of "standard" FS-LIB spark behavior.

The motion of the centroid of the spark occurred mostly in the direction of beam propagation. As indicated previously, the direction normal to beam propagation will be given as the x-axis and the direction of beam propagation will be given as the Y-axis in future figures and tables. The motion in the X-axis was less than two microns in each run collected, which is less than a tenth of a pixel when referenced to the image pixel size, and likely could be noise as much as actual movement. Table 3.1 shows the average motion in the X and Y axes as well as the standard deviation in each run when compared to that run's mean image. All of this data was averaged together to give the values in the last row of the table. For a nanosecond LIB spark, Rennie et.

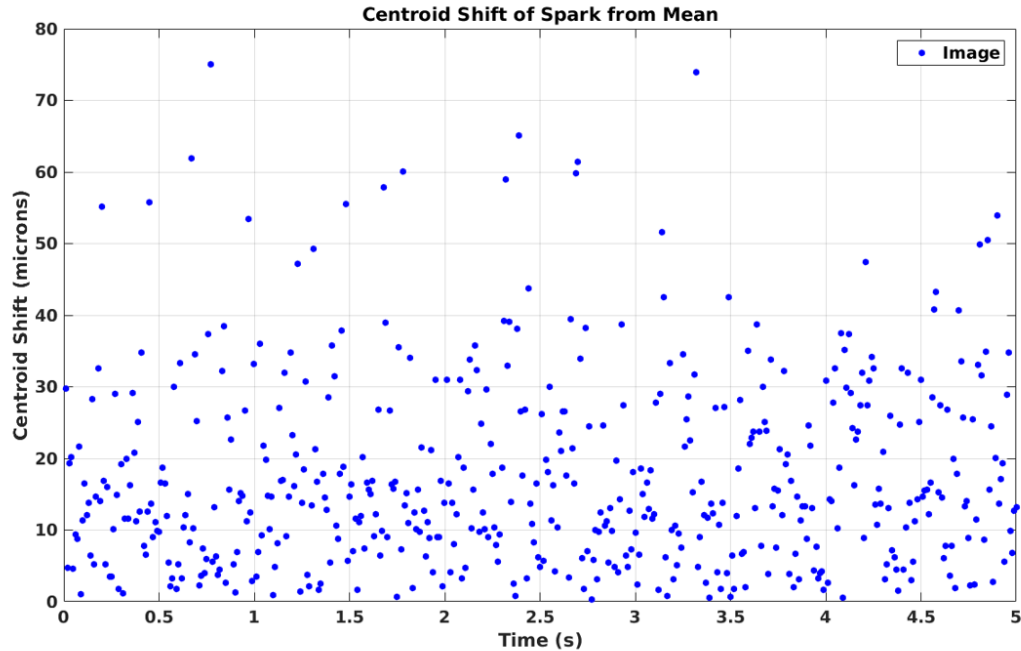


Figure 3.2: The Norm of the Displacement of the Spark Centroid from the Mean Image over the Course of One Run

al. reported an average displacement in the direction of beam propagation of approximately 80 microns and an average displacement normal to beam propagation of approximately 10 microns[4], so the FS-LIB spark’s centroid displacement is approximately one fifth that of a nanosecond LIB spark as reported in prior literature. It is worth noting that prior literature shows the centroid displacement has a dependence on both laser energy above the breakdown threshold as well as the  $f/d$  ratio of the focusing optics used to generate the spark. However, the trends are not all linear for every case plotted, so the approximate average value for all cases was selected for comparison to the results shown in this work.

In addition to the motion of the spark centroid, the spark width, height, and area change were also calculated when compared to the mean image from each run. Figures 3.3 and 3.4 show the percent change in spark width and height, respectively. This is referenced to the overall

Table 3.1: Spark Centroid Motion in the X and Y Axes

Run Number	X-Disp(Average, $\mu\text{m}$ )	X-Disp(STD, $\mu\text{m}$ )	Y-Disp(Average)	Y-Disp(STD)
FS-BB-01	2.06	1.34	17.29	12.36
FS-BB-02	1.62	1.41	18.21	12.22
FS-BB-03	1.98	1.27	17.30	12.36
FS-BB-04	1.48	1.44	17.43	12.12
FS-BB-05	1.56	1.32	16.30	12.14
FS-BB-06	1.44	1.34	16.75	12.09
FS-CF-01	2.15	1.67	17.02	11.96
FS-CF-02	1.57	1.20	18.40	13.52
FS-CF-03	1.74	1.12	16.32	12.36
FS-CF-04	1.66	1.21	18.78	13.48
FS-CF-05	1.45	1.23	17.19	13.32
AVG	1.70	1.32	17.36	12.54

width and height of the spark in the mean image. The average width change was approximately two percent of the total spark width, and the average height change was approximately three percent of the total spark height. Like the centroid shift, these changes are very small compared to the size of the spark, and cannot be seen without a camera with a zoom lens and some image processing. The spark area change, as shown in Figure 3.5, is likewise very small, on the order of two to three percent of the total spark area in the reference image. These values correspond to around a 20 to 30  $\mu\text{m}$  change in spark dimensions pulse-to-pulse. The small percent changes in spark dimensions mean that any error introduced by the spark's size and shape could be largely removed through mean-subtraction or a similar technique.

Overall, the movement and size change of the spark from pulse to pulse is very small when compared to the actual size of the spark itself. This is promising since smaller deviations in these parameters from the mean should correspond to smaller amounts of addition wavefront error introduced by using the spark as a source when compared to a collimated source. The change in spark centroid location appears to be almost entirely in the direction of beam propagation, and

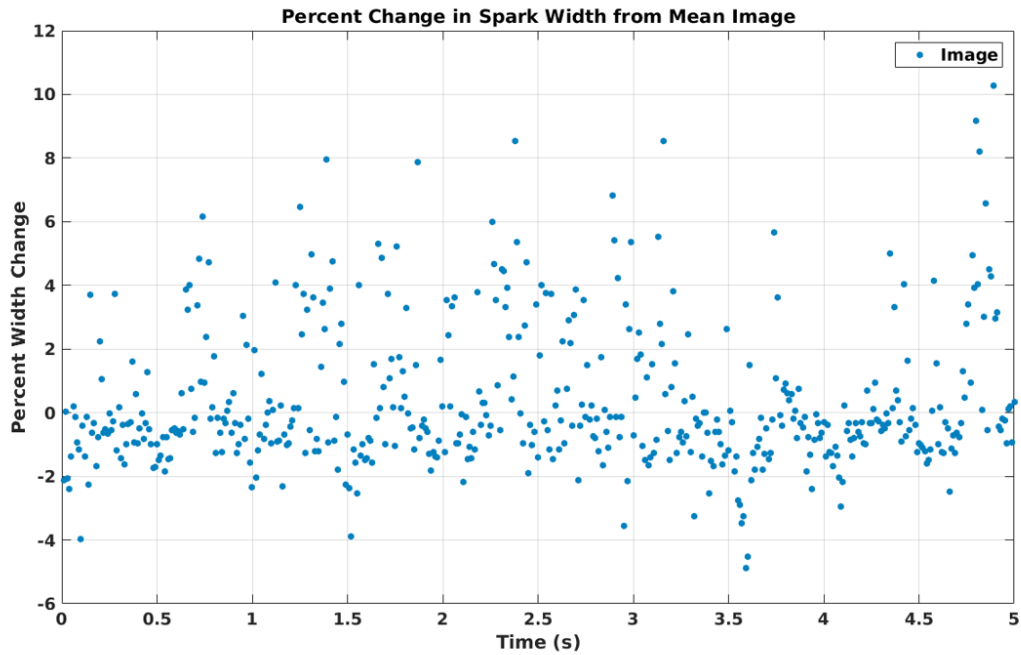


Figure 3.3: The Percent Width Change of the Spark from the Mean Image over the Course of One Run

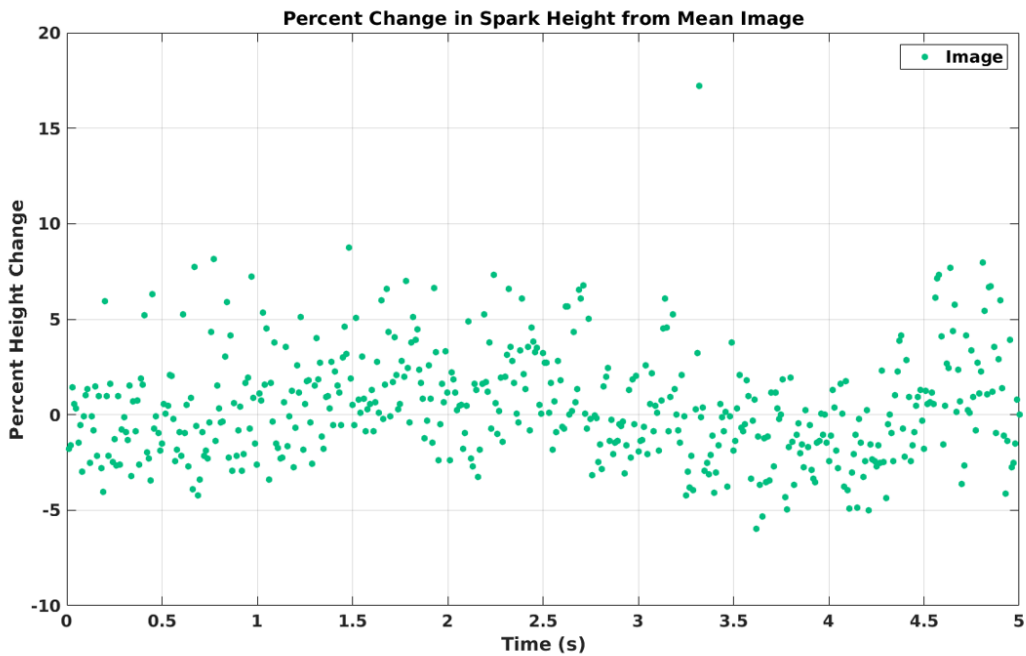


Figure 3.4: The Percent Height Change of the Spark from the Mean Image over the Course of One Run

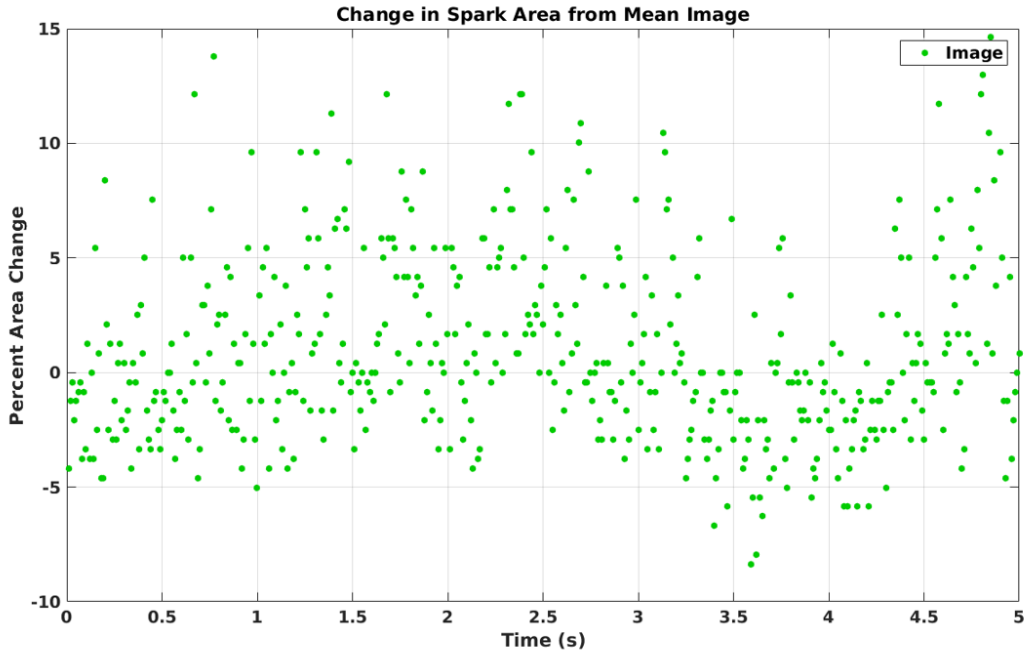


Figure 3.5: The Percent Area Change of the Spark from the Mean Image over the Course of One Run

the change in spark height is also much greater than the change in width.

### 3.2 Wavefront Tip and Tilt

As mentioned in section 2, after processing the wavefronts from the spark, the tip and tilt from each mean-subtracted wavefront was calculated. This was done for both the wind-off and wind-on data collected. Typically, during data processing the tip and tilt are removed from the final wavefronts since flow features like turbulence produce higher-order aberrations[24], and therefore if the FS-LIB spark introduces additional tip and tilt it can be removed before parameters such as  $OPD_{rms}$  are calculated. An example trace of tip and tilt before the start of a run is shown in Figure 3.6, which demonstrates the presence of both parameters without the contribution of additional wavefront error created by a moving flowfield. Here the tilt present in

the wind-off wavefronts is about an order of magnitude greater than the tip, which is similar to the difference in the spark centroid's shifts in the x- and y-directions. This can be compared to the time trace during the wind-on "good flow" period for the same run as shown in Figure 3.7. This set of traces shows a similar range of magnitudes as the wind-off trace, indicating that the tip and tilt measured in the wind-on wavefronts does not come primarily from the flow features present but rather from the spark itself. The average wind-on magnitudes for wavefront tip and tilt are given in Table 3.2. Here, it is again apparent that the tip value is about an order of magnitude lower than the tilt.

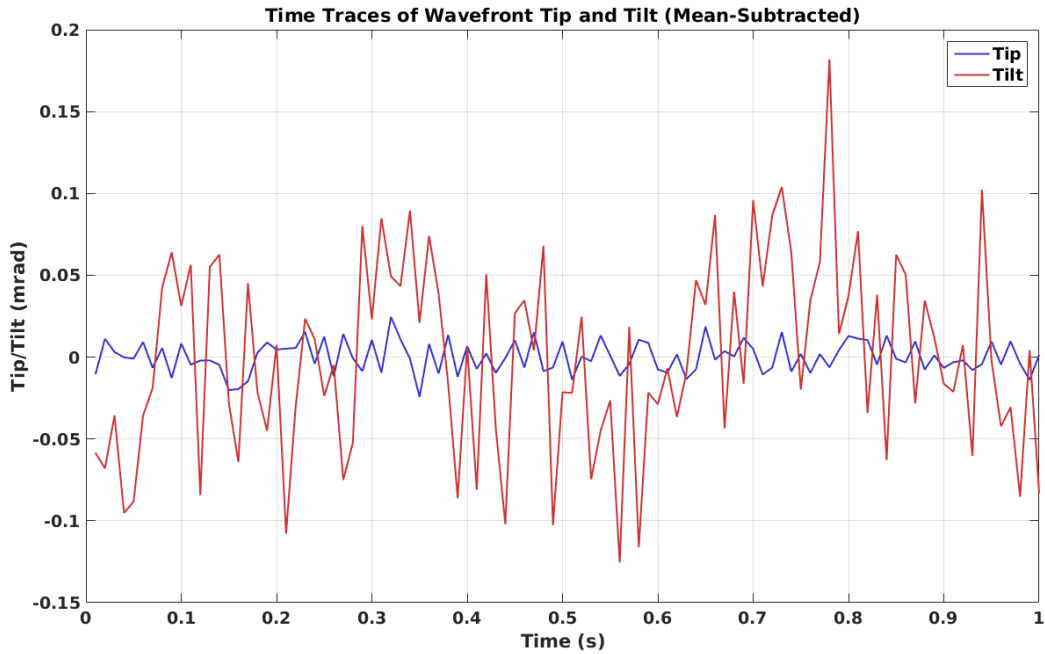


Figure 3.6: The Wavefront Tip and Tilt Present Before a Run Using the FS-LIB Spark

Table 3.2: Average Tip and Tilt Magnitudes (Wind On)

Tip (mrad)	Tilt (mrad)
0.007	0.047

As an additional check to determine if the instantaneous wavefront tip and tilt are in fact

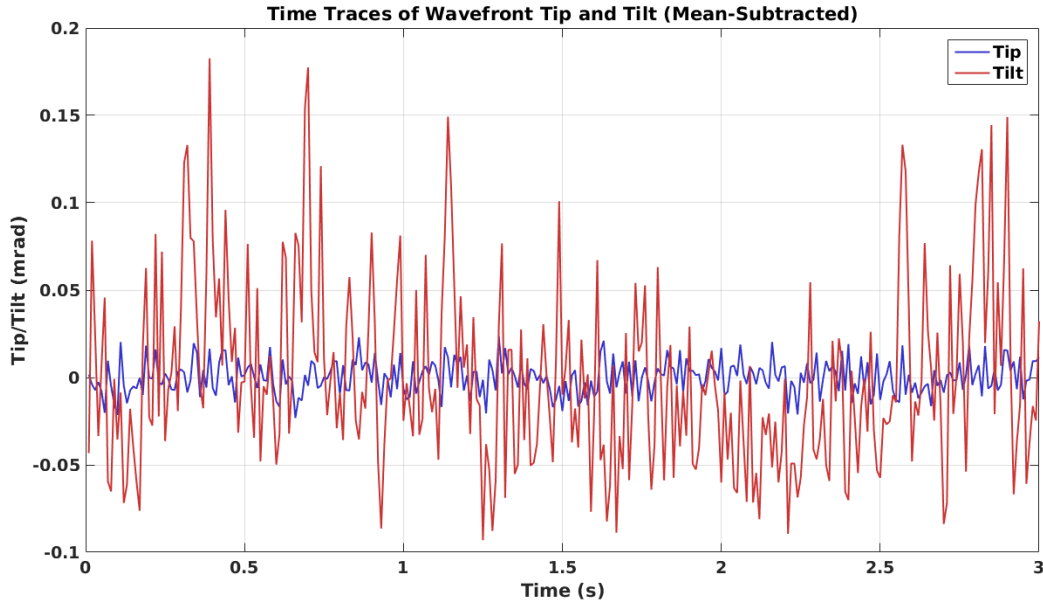


Figure 3.7: The Wavefront Tip and Tilt Present During One Run Using the FS-LIB Spark

coming from the spark, the tip and tilt from the spark wavefronts were plotted against the motion of the spark centroid. Figures 3.8 and 3.9 show the comparison between the centroid motion and wavefront tip and tilt for all of the wind-off data collected. Here, even though it was shown in the previous figures that the flow features do not contribute to the instantaneous tip and tilt, the following figures nonetheless show wind-off data to ensure that no flow-related tip and tilt affects the correlations generated. The  $R^2$  values shown on the plots are for all of the data plotted and not averages of the individual run  $R^2$  values. From these results, it appears that there is little correlation between the motion of the spark centroid in the x-direction and the wavefront tip. However, this may be due to the fact that the x-shift of the centroid was extremely small, to the point where it was within a fraction of a pixel of the camera. This points to the calculated x-shift being as much from processing error or camera noise as from actual spark motion. The wavefront tip is correspondingly small and could also likely be as much camera noise as it is actual measured data. In contrast, the y-shift of the spark centroid appears to have a distinct

correlation to the wavefront tilt in each image. A collection of  $R^2$  values for each run is shown in Table 3.3 for the M3T. Since all of the wavefronts used for this analysis have already had a mean tare image subtracted out of them, the correlation between the wavefront tilt and the spark centroid motion indicates again that the instantaneous tip and tilt are produced by the spark itself and are not from flow features created in the M3T.

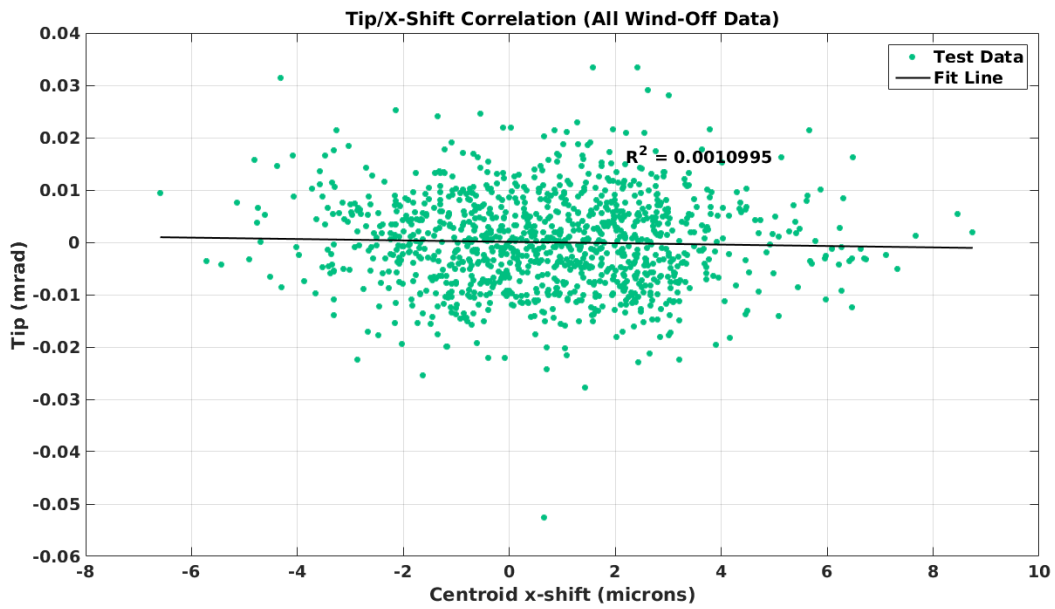


Figure 3.8: The Relationship Between Wavefront Tip and Spark Centroid X-Displacement

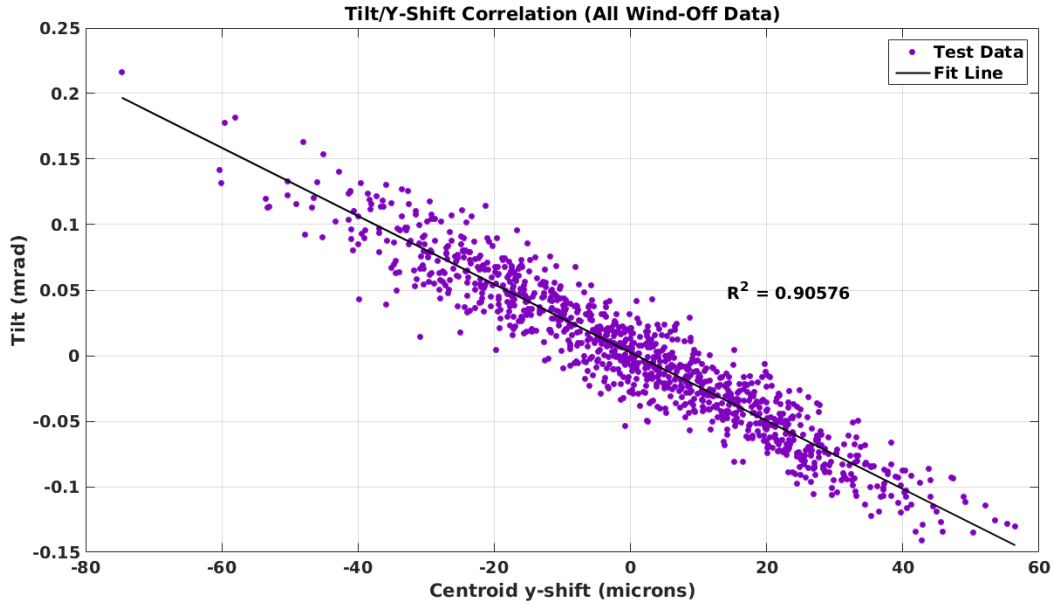


Figure 3.9: The Relationship Between Wavefront Tilt and Spark Centroid Y-Displacement

Table 3.3: Spark Centroid Motion to Wavefront Tip/Tilt Correlation Strength by Run

Run Number	R <sup>2</sup> Tip	R <sup>2</sup> Tilt
FSCF01	0.00	0.92
FSCF02	0.00	0.91
FSCF03	0.02	0.91
FSCF04	0.00	0.92
FSCF05	0.00	0.92
FSBB01	0.04	0.94
FSBB02	0.02	0.90
FSBB03	0.00	0.91
FSBB04	0.01	0.87
FSBB05	0.01	0.92
FSBB06	0.03	0.93

### 3.3 Spark Dimension Change with Pressure

In addition to the primary data taken with the spark at atmosphere, a series of images were taken of the spark in a vacuum cell at different pressure levels to determine the role the air density

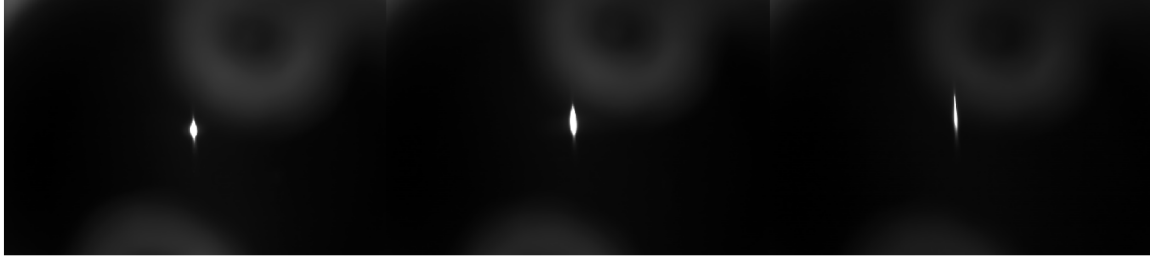


Figure 3.10: The FS-LIB Spark Generated at Various Ambient Pressures. From left to right: 760 torr, 100 torr, and 10 torr.

(controlled by the pressure change) plays in the spark properties. Since not every test facility where aero-optic data is collected operates with an atmospheric static pressure, understanding how the spark's dimensions will change due to a pressure drop in a moving flowfield is important. Figure 3.10 shows a sequence of images of the spark at various pressure levels inside the vacuum cell, and Figure 3.11 show the change in spark height and width with changing pressure. Overall, as pressure decreases, the spark height increases and width decreases, to the point where the spark is about twice as tall and half as wide at 10 torr as it is at atmospheric pressure. In addition, the change does not appear to be linear. The "stretching" of the spark appears to occur much more rapidly at pressures below 100 torr. This means for a facility operating with freestream pressures at these levels, taking tare images of the spark at approximately the run freestream pressure will be especially important to capture the wavefront errors introduced by the spark's shape at that pressure level.

Perhaps even more interesting is the behavior of the spark pulse-to-pulse as ambient pressure is decreased. Figure 3.12 shows the change in the FS-LIB spark's average centroid displacement from the mean with changing ambient pressure. The average motion of the spark's centroid decreases significantly at lower pressures, to the point where the centroid displacement is only a few microns at ambient pressures below about 80 torr. This indicates that the spark is becoming

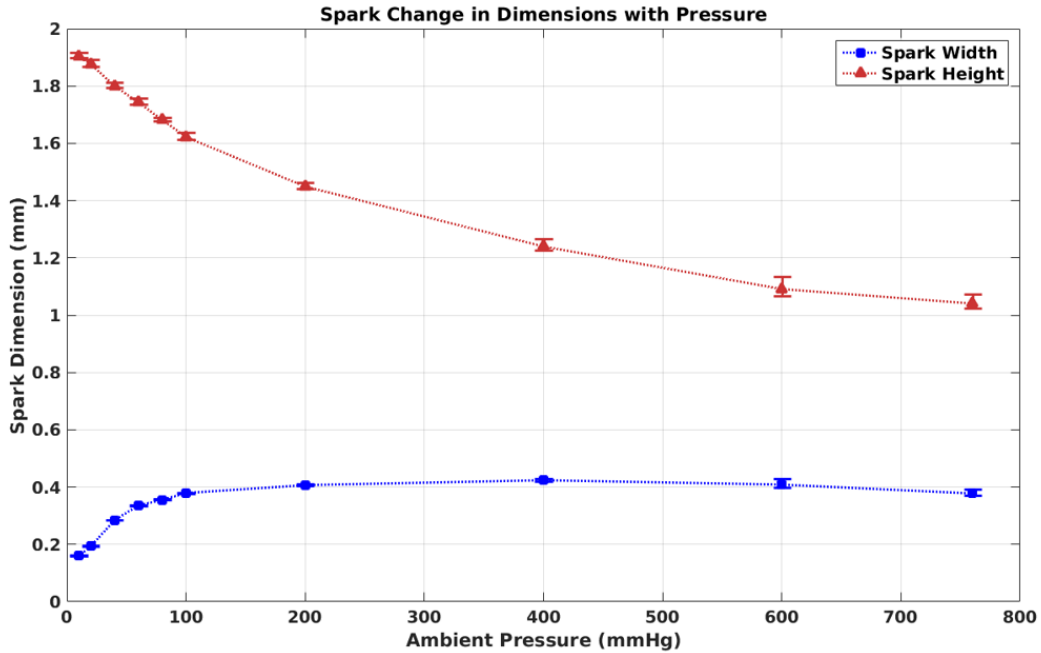


Figure 3.11: The FS-LIB Spark Dimension Change with Pressure

more stable as the ambient pressure decreases, meaning that if the spark is to be used in a lower pressure environment its utility as an aero-optic source may be much higher. Neal et. al. collected similar data on a nanosecond LIB spark at a pressure of approximately 30 torr and found a centroid displacement close to 50 microns[21] using a much more comparable optical setup to that presented in this work, meaning that at low pressures the relative performance of the FS-LIB spark compared to a nanosecond LIB spark appears to be better as well. One possible explanation for this is that the pulse energy above the breakdown threshold is decreasing since the density of the target gas is decreasing as well, which would agree with the results from studying nanosecond LIB sparks in prior literature[4]. Another possible explanation is that, at low densities, the emission observed is created more by femtosecond filamentation and less by full breakdown.

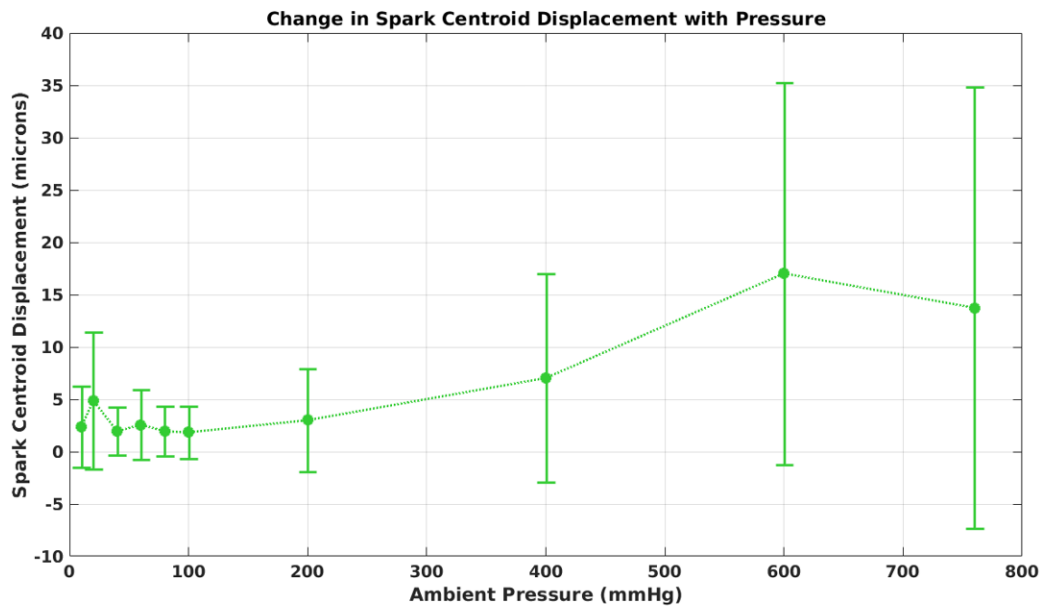


Figure 3.12: The FS-LIB Spark Average Centroid Displacement Versus Pressure

## Chapter 4: Results: Spark Wavefront Analysis

### 4.1 Spark Wavefronts

An example of the raw wavefront sensor images collected during a run using the spark as a source is shown in Figure 4.1. As can be seen, the overall illumination from the FS-LIB spark is fairly uniform. There is some minor defocusing towards the edges of the lens array grid, but this is likely due to imperfections in the optical setup and therefore can be subtracted out with the use of tare images. Since the FS-LIB spark is not a perfect point source but rather has finite size, the resultant focal spots seen on the detector are also several pixels across. On average, each focal spot from the FS-LIB spark is approximately twenty by twelve pixels on the detector. It is worth noting here that the missing set of focal spots in the corner of this raw image is an artifact of the camera setup itself not reading that set of pixels and not due to poor alignment of the optics used in the experiment. They do not affect the wavefront data shown in this chapter since the raw images are cropped slightly when they are fed into the primary data reduction code. This also removes the most out-of-focus portions of the lens array from the analysis, and in the case of the CW source removes the less well-illuminated portions of the raw image. Approximately 40 by 29 microlens images can be seen in the raw image, of which 34 by 23 are kept for final processing.

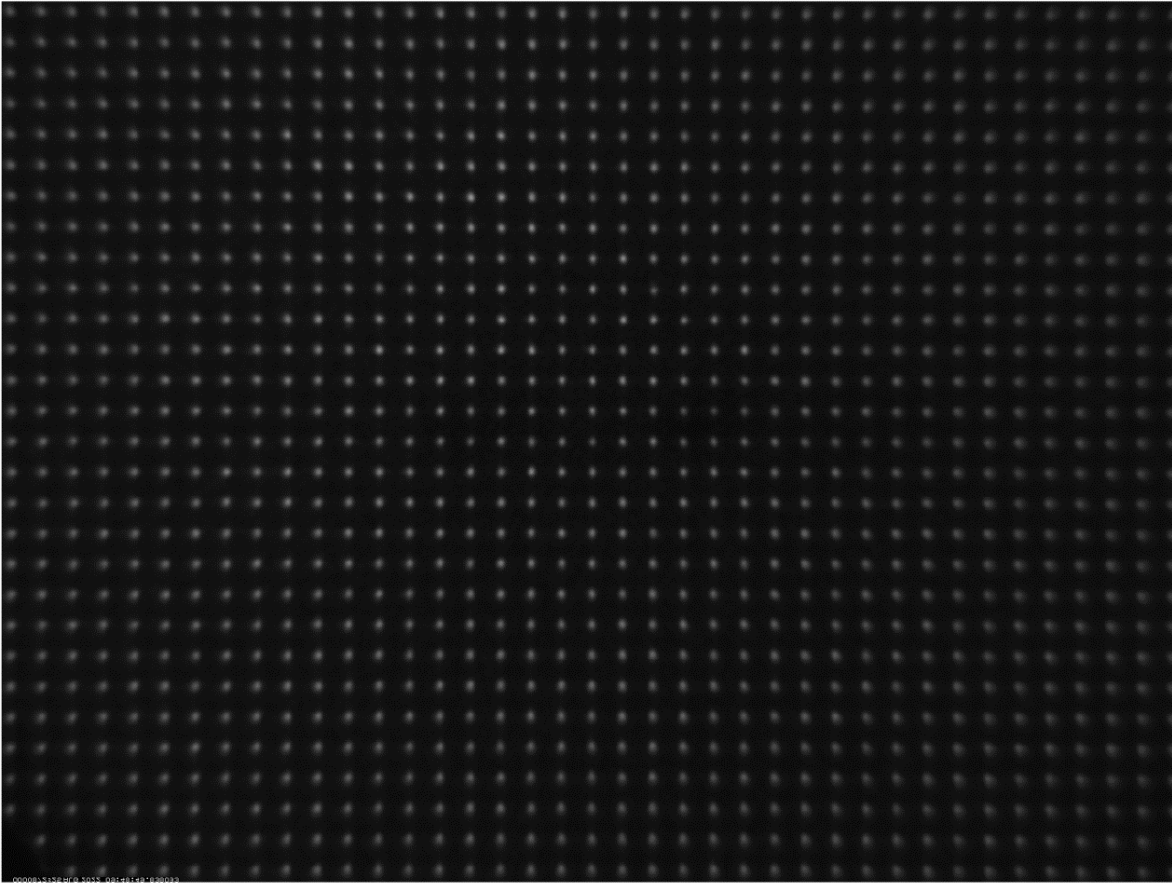


Figure 4.1: An Example of the Raw Wavefront Sensor Images

Figure 4.2 shows an example of a mean-subtracted wavefront produced using the FS-LIB spark as the source of illumination. This image has had the wavefront tip and tilt removed to leave only higher-order distortions created by flow turbulence behind. Qualitatively, the peak-to-valley distance between features in this image are approximately ten millimeters across, given that each grid square represented is 500 microns to a side. This indicates that the features seen here could in fact be turbulence produced by the boundary layer, since their size is on the order of the boundary layer thickness in the M3T. The wind-off image in Figure 4.2 does not show the same large-scale

features, lending further evidence to this. Smaller peaks and valleys in the wind-on wavefront are likely a mixture of both real flow features and noise from the wavefront sensor itself. Since multiple sources of turbulence were being imaged simultaneously during each run, the smaller features are also possibly remnants of multiple turbulent structures being superimposed over one another and appearing to add constructively or destructively to one another in the total wavefront error. The sample rate of the experimental setup was not high enough to image the same turbulent structure multiple times as it moved through the aperture, so confirming definitively that these are in fact turbulent features is not possible from looking at the wavefront itself. However, subsequent analysis of the spatial  $OPD_{rms}$  for both the FS-LIB spark and the collimated source indicate that the distortions captured are from the flow.

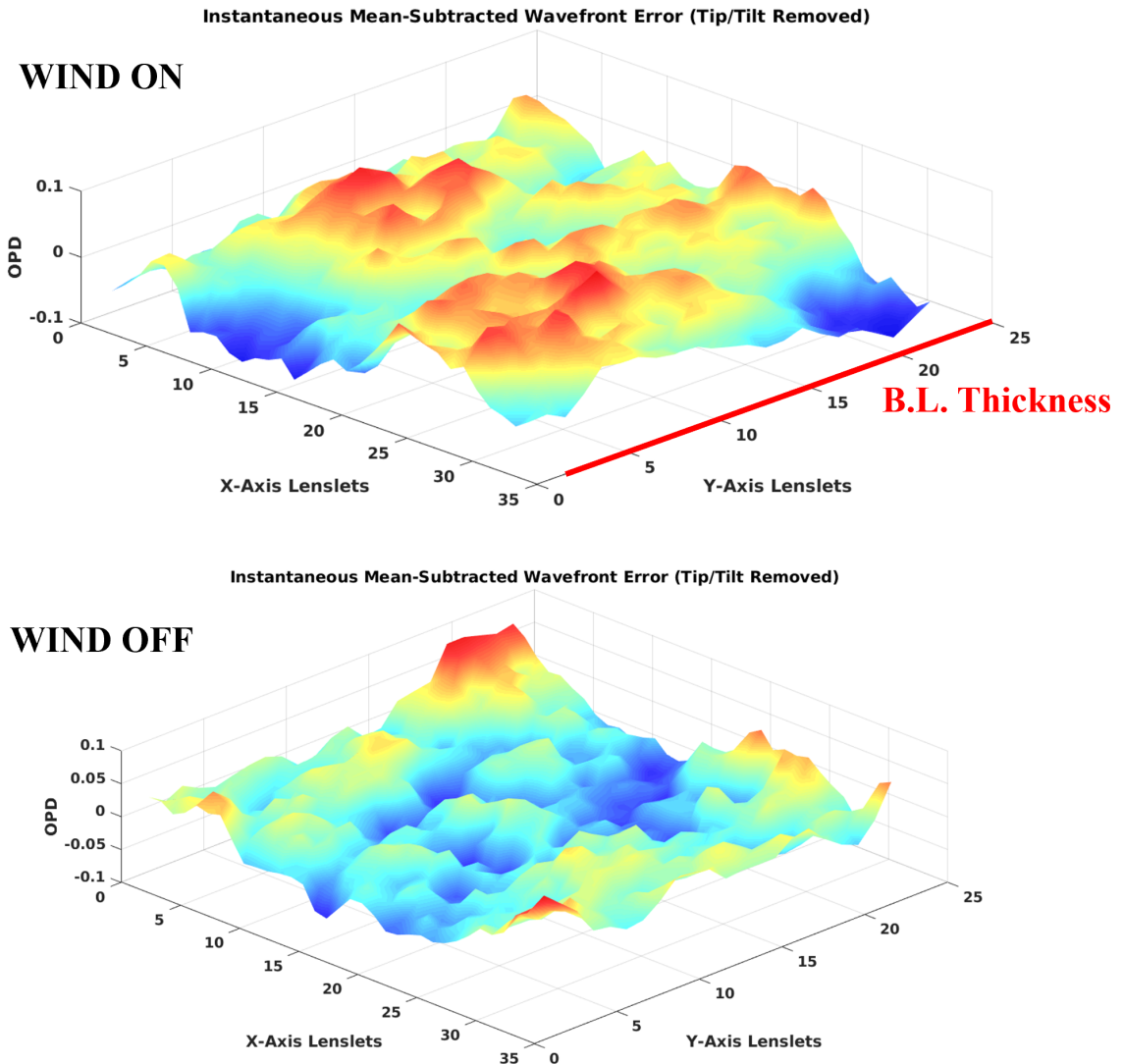


Figure 4.2: Examples of Instantaneous Wavefronts Imaged With the Spark. The Wind-On Wavefront Shows Additional Distortions that Could be Related to Boundary Layer Turbulence

These instantaneous wavefronts with the tip and tilt removed were used to generate time traces of the wavefront  $OPD_{rms}$  for each run. This analysis was performed both over the full run time captured as well as for just the steady "good flow" period of the tunnel. Examples of the  $OPD_{rms}$  time traces for two runs are shown in Figure 4.3 and Figure 4.4. The second trace is from a run with the blunt body installed in the tunnel and the camera recording time stretched to ten

seconds to capture the unstart of the tunnel at the end of the run. The prominent changes to the flow state are labeled in Figure 4.4. The establishment of supersonic flow in the M3T can be seen approximately one second after recording begins, where the distortions created ramp up before spiking briefly. Here, the non-zero  $OPD_{rms}$  value before significant flow is moving through the tunnel is likely a mixture of noise from the camera setup as well as possible additional wavefront error introduced by the FS-LIB spark. As steady flow is established, the  $OPD_{rms}$  levels off at a roughly constant, slightly higher value. In the extended run, a second, more pronounced spike in wavefront distortion occurs approximately eight seconds into the run, corresponding to the unstart of the tunnel at this point in time. The time traces also show the variation in the spatial  $OPD_{rms}$  from wavefront to wavefront, which shows up in both the FS-LIB spark data and the collimated source data to varying degrees through all runs.

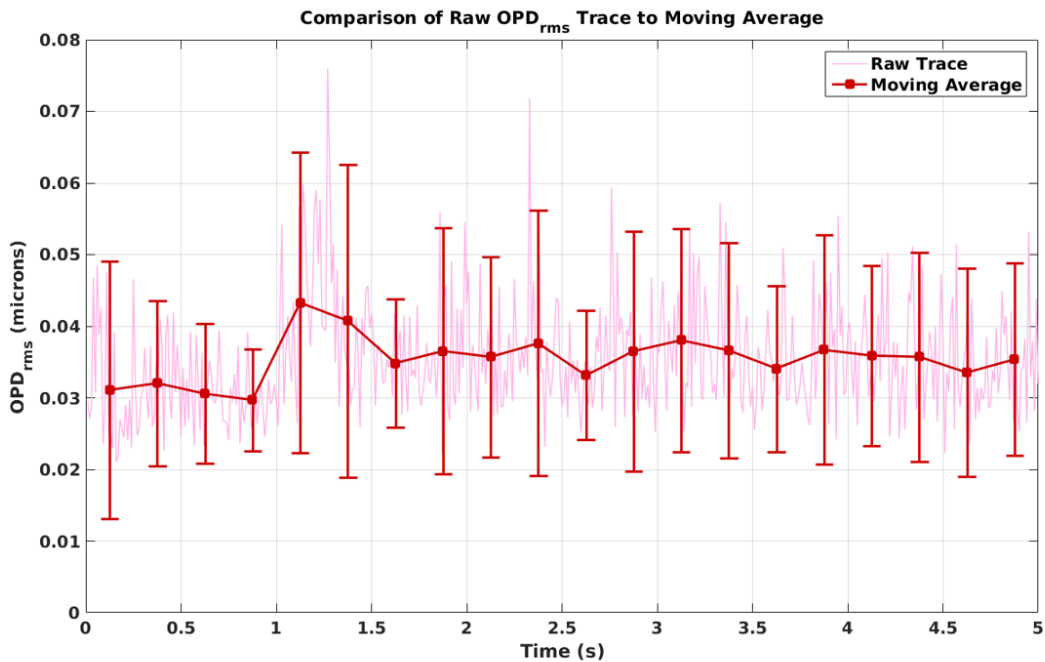


Figure 4.3: An Example Time Trace of  $OPD_{rms}$  During Tunnel Startup and Good Flow of an Empty Tunnel Run with a Moving Average Overlaid

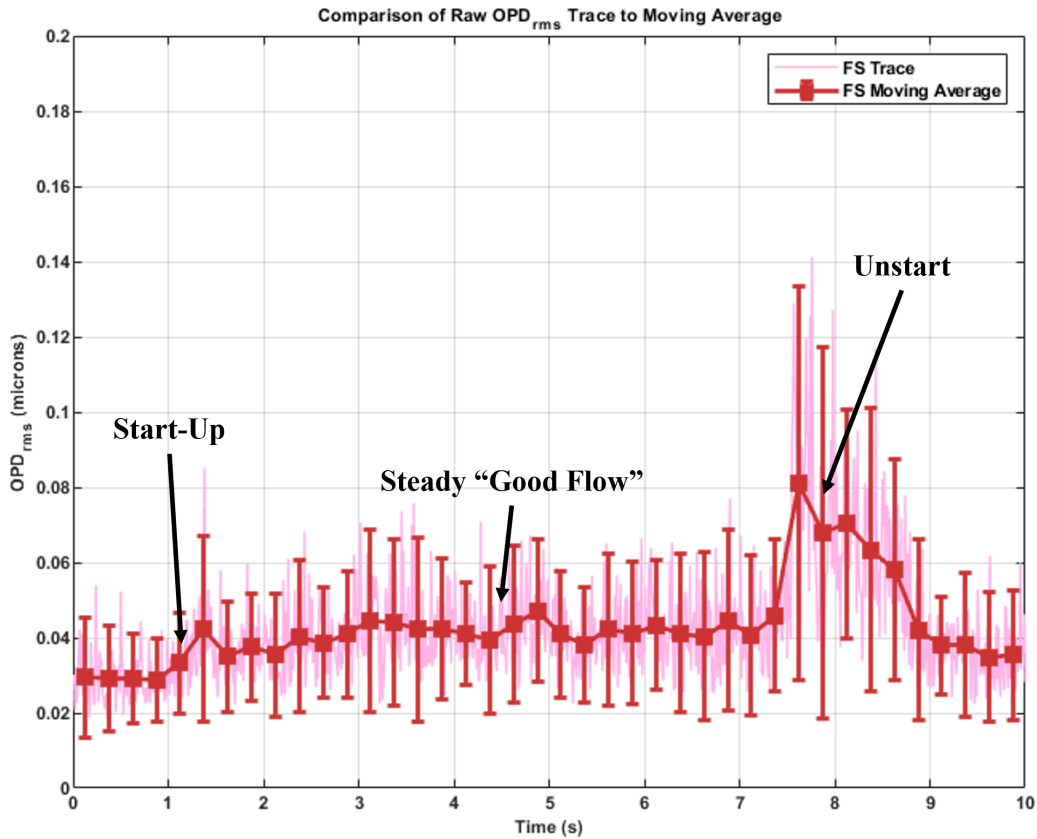


Figure 4.4: An Example Time Trace of  $OPD_{rms}$  for Startup, Good Flow, and Unstart of an Extended Run with the Blunt Body Installed in the Tunnel

## 4.2 Comparisons to Collimated Laser Wavefronts

As mentioned previously, in addition to the runs where wavefront data was collected using the FS-LIB spark, several runs were collected with the use of a collimated laser beam as the source. The use of the collimated source provides a reference to which the FS-LIB spark wavefronts can be compared, since the collimated laser source is the established approach to collecting wavefront data for aero-optic applications. A comparison of the raw time traces from one CW source run and one FS-LIB spark run are shown in Figure 4.5. Here, the biggest difference between the two traces appears to be in the beginning of the run before supersonic flow is

established. The CW source measures a much lower  $OPD_{rms}$  threshold and its trace shows less variation in the spatial  $OPD_{rms}$  from wavefront to wavefront before flow is fully established in the M3T. However, once good flow is established, the two traces are much closer, with the collimated source appearing to produce an  $OPD_{rms}$  just below that of the FS-LIB spark.. This suggests that any additional wavefront error added by the FS-LIB spark does not add linearly to the distortions created by flow features. In addition, the standard deviation measured for both sources appears to be similar during the wind-on "good flow" period as does the spatial  $OPD_{rms}$  variation.

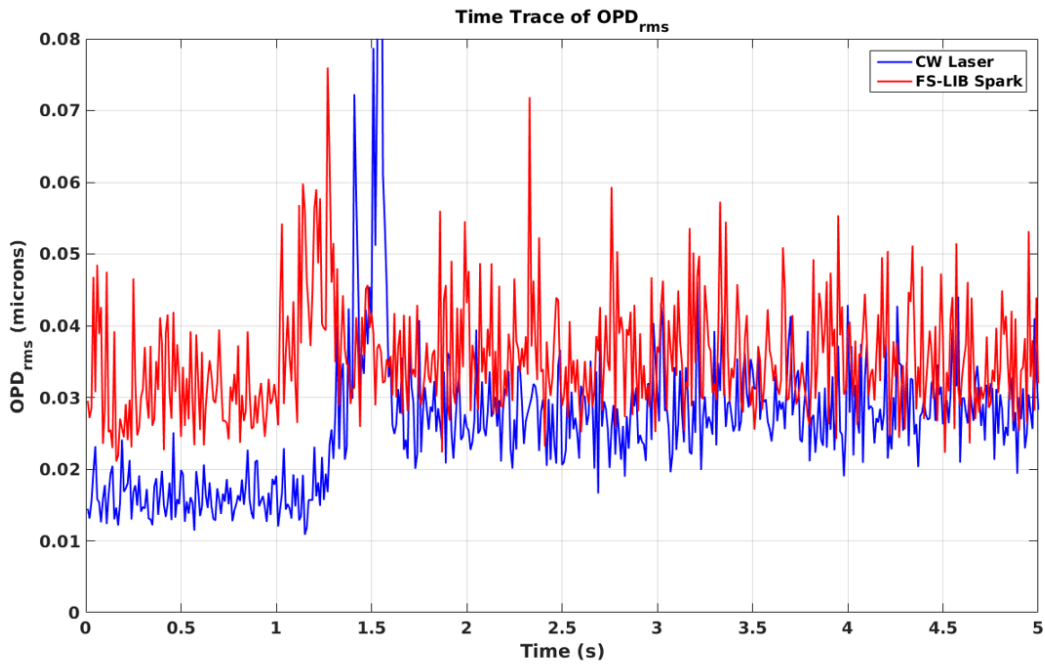


Figure 4.5: An Example Comparison of  $OPD_{rms}$  Time Traces

To take a closer look at the relative performance of the two sources, a moving average of every 25 wavefronts was computed and added to the time trace plots. The standard deviation was also computed and used to approximate the uncertainty in the moving average. The tunnel run was also broken into stages for examination, beginning with start-up, then moving to the steady "good flow" period. Figure 4.6 shows the two moving averages with the time traces overlaid

in the background for reference. This close-up of the first hundred images better shows the difference between the two sources with no or little flow present. At this stage it is unlikely that any sort of turbulent boundary layer has formed on the tunnel walls, so the  $OPD_{rms}$  shown here is most likely a mix of camera noise, inconsistencies in the emitted intensity of the collimated source, and error introduced by the FS-LIB spark's motion. It is worth noting that, when the uncertainties are included, the two source  $OPD_{rms}$  traces still almost overlap, so even without any flow-related disturbances present the difference created by the FS-LIB spark is statistically insignificant. More interesting is the much larger standard deviation in the time trace itself when using the FS-LIB spark versus the collimated source.

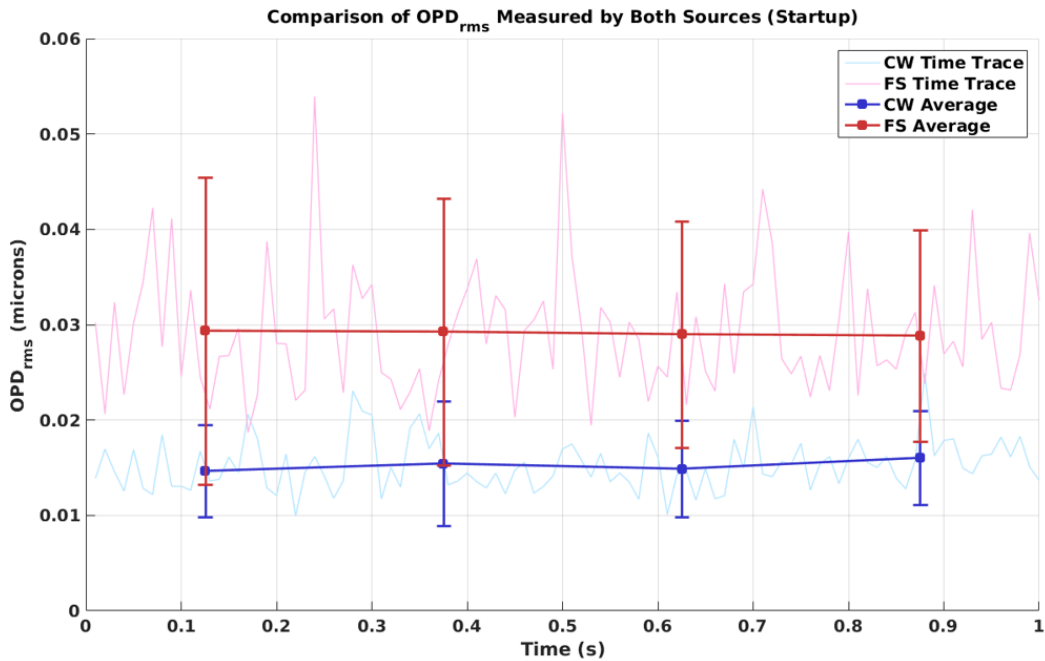


Figure 4.6: A Comparison of the FS-LIB Spark and CW Source  $OPD_{rms}$  Moving Averages (Tunnel Start-Up)

Next, the steady 'good flow' period was examined. The good flow only time traces from all FS-LIB spark runs were combined into a single moving average, with a similar analysis being

done on all of the collimated laser source runs. Note that, since two tunnel configurations were tested, this process was performed for each configuration separately. A comparison of all of the results is shown in figure 4.7 for the runs where only the tunnel wall boundary layers were analyzed. As shown, the FS-LIB spark shows a slight increase in average  $OPD_{rms}$  compared to the CW laser. However, the ninety-five percent confidence intervals for the two sources still overlap, indicating that the difference in wavefront error as introduced by the spark is not statistically significant. In addition, the standard deviation seen for the averaged runs is similar. This is unlike the startup traces shown previously, where the collimated laser showed a smaller standard deviation than the FS-LIB spark trace. Figure 4.8 shows the average of all good flow data for both sources when the blunt body was installed in the tunnel. For these runs, the two traces lie almost on top of one another. There are still slight differences, which could come from a number of sources, including the slight difference in overall imaged area between the two sources. As mentioned in chapter 2, the FS-LIB spark has a smaller aperture size on the window closest to it compared to the collimated laser. This is because it acts as a point source rather than a "line-of-sight" source. This would explain why the collimated laser now measures a slightly higher overall  $OPD_{rms}$  where previously it reported a slightly lower value. Both of these plots indicate that the flow features such as turbulence, when present, dominate the wavefront error measurement, to the point where the differences associated with the light source are insignificant.

To examine the relative response of the two sources in more detail to changes in flow conditions and the resulting aero-optic aberrations, a comparison of runs where the tunnel was allowed to run until unstart occurred was done as well. The two time traces with their moving averages are shown in Figure 4.9. Here the wind-on wavefront traces for the two sources are again similar, even as the tunnel begins to unstart and supersonic flow breaks down. The initial start-up

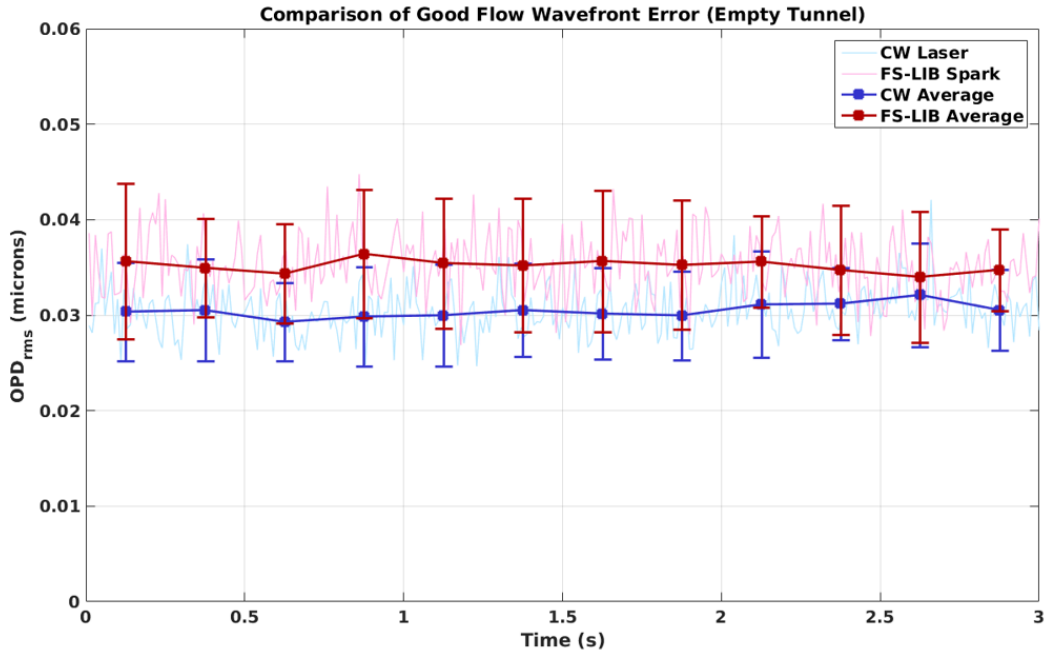


Figure 4.7: A Comparison of the FS-LIB Spark and CW Source  $OPD_{rms}$  (Empty Tunnel)

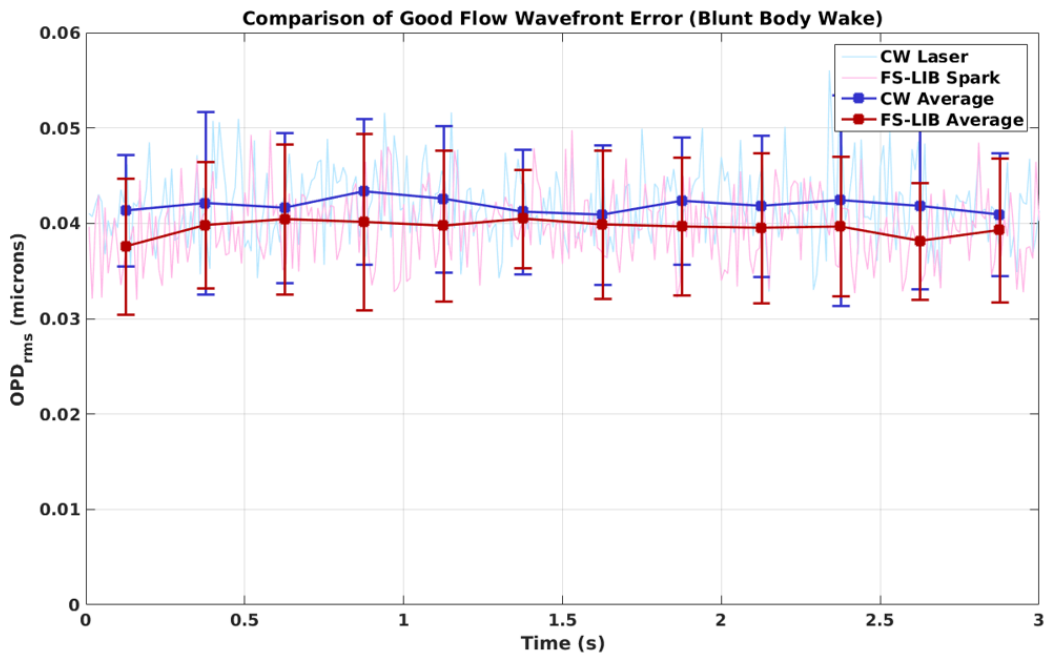


Figure 4.8: A Comparison of the FS-LIB Spark and CW Source  $OPD_{rms}$  (Blunt Body Present)

phase of the tunnel appears to be better-captured once again by the collimated source, with a more pronounced increase in the wavefront aberrations as supersonic flow is established around 1.5 seconds and a lower image-to-image deviation in the first second of the measurement. This is consistent with the previously shown data, which indicates that any additional aberrations created by the FS-LIB spark are most noticeable with no or little flow present. The steady "good flow" period shows roughly the same values as shown previously for the blunt body data with shorter data acquisition times. As the tunnel unstarts, the sharp increase in aero-optic distortions due to the unstart process seems to be captured to the same degree of fidelity with both sources. Overall, this again indicates that, if there is additional noise introduced into the wavefront measurement by the FS-LIB spark, it does not significantly affect the spark's ability to function as an illumination source for aero-optic aberrations created by flow features. The additional spark error seems to be predominantly present in data where no other significant sources of wavefront error are being detected by the wavefront sensor.

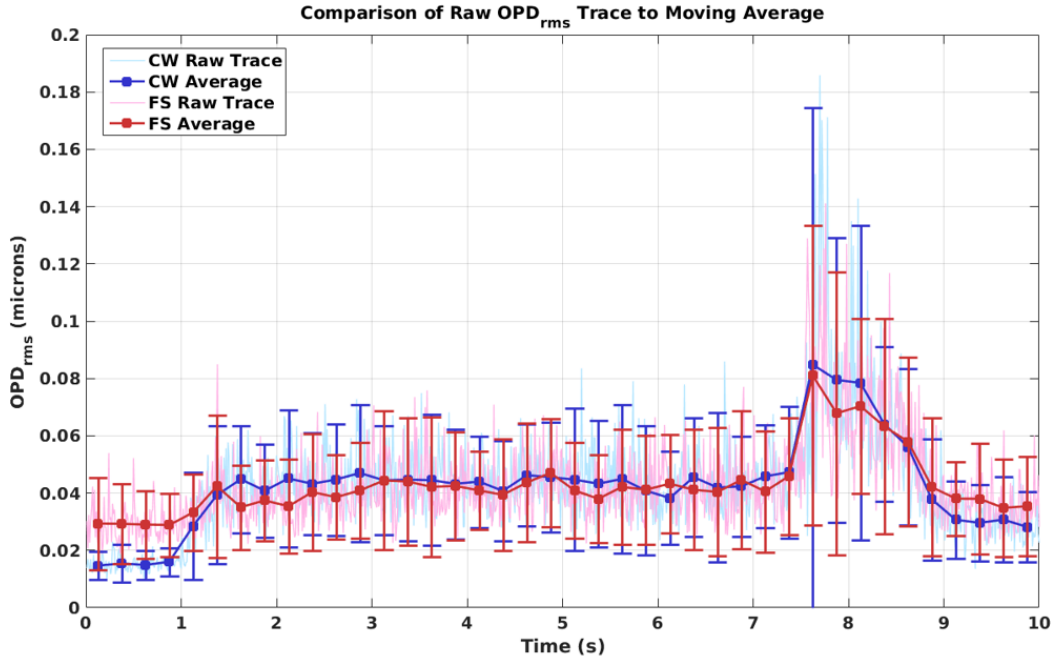


Figure 4.9: A Comparison of the FS-LIB Spark and CW Source  $OPD_{rms}$  (Extended Runtime)

### 4.3 Spark Wavefront Modal Analysis

In order to compare the FS-LIB spark further to the nanosecond-LIB spark, a series of modal analyses were performed on the wavefront data similar to that presented in Nguyen et. al. for the nanosecond LIB spark[25]. First, a Zernike mode analysis was performed on the FS-LIB spark wavefronts to determine what, if any, dominant Zernike modes exist in them. These were then compared to the Zernike modes present in the wavefronts collected using the collimated laser source. Zernike modes are often used to reconstruct wavefronts in optical systems due to their ability to represent "classical" optical aberrations, such as defocus or astigmatism. Figure 4.10 shows the relative strengths of the first twenty-one Zernike modes for both the collimated laser source and the FS-LIB spark. These results were generated using the tip/tilt removed wavefronts shown previously. Overall, there is a slight increase in the amplitude of each Zernike mode for the

FS-LIB spark compared to the collimated laser. However, unlike what has been observed in prior literature with a nanosecond LIB spark, there do not appear to be any dominant Zernike modes present in the FS-LIB spark wavefronts that are not in the collimated laser wavefronts. Note that there still appear to be tip and tilt (modes 2 and 3) present in the wavefronts studied even though these wavefronts had their overall tip and tilt removed. This is likely due to the fact that the Zernike mode analysis was performed on a circular sub-region of each wavefront. Zernike mode basis functions are generated over a unit disk, so the region of an image they can be applied to must be circular, which is what drove this restriction. Since the tip/tilt removal was performed over the total wavefront, the tip and tilt may not be perfectly removed in the sub-region sampled.

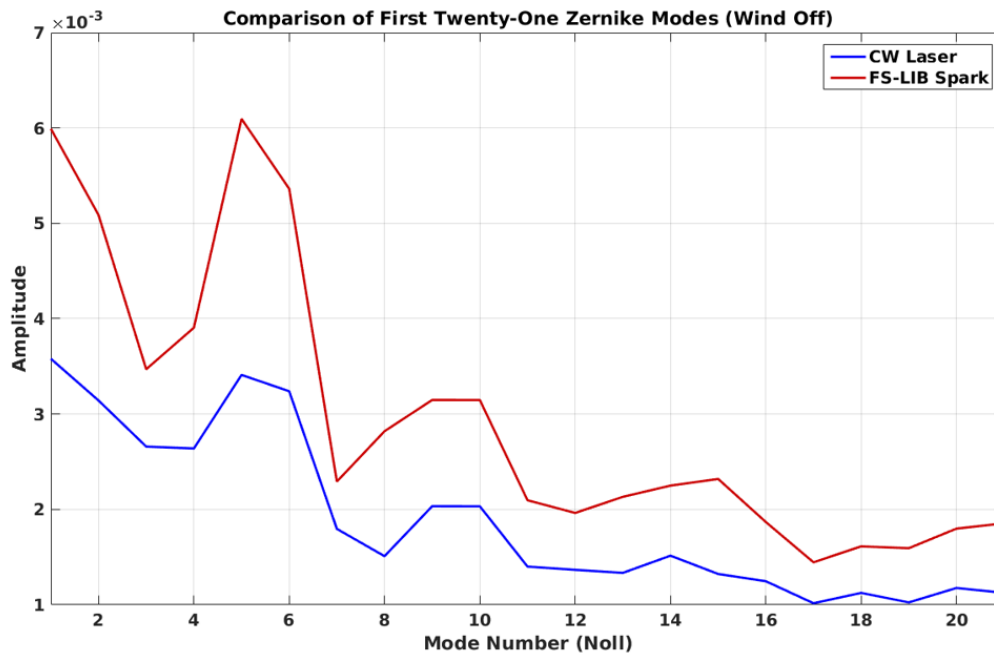


Figure 4.10: The dominant Zernike modes for the CW Laser and FS-LIB Spark Wavefronts (Tip/Tilt Removed)

Additionally, the FS-LIB spark and collimated laser wavefronts were deconstructed using Proper Orthogonal Decomposition and the shapes of the dominant POD modes were compared.

Figure 4.11 shows the first POD mode from each source. The biggest revelation here is that the POD analysis shows a distinct mode shape common to all of the run data collected using the FS-LIB spark. This mode shape resembles several Zernike modes combined, which agrees with the overall increase in Zernike mode coefficient amplitudes seen previously for the FS-LIB spark versus the collimated laser. This also agrees with the slight increase in  $OPD_{rms}$  as measured using the FS-LIB spark versus using the collimated laser. Additionally, this is similar to results published in literature for a nanosecond LIB spark. The nanosecond LIB spark produces an additional wavefront error consisting of several Zernike modes when viewed orthogonally, and the overall mode shape produced by POD is somewhat similar to the mode shape from the FS-LIB spark[25], albeit rotated approximately 45 degrees. This POD mode could potentially be removed from the FS-LIB spark wavefront data in order to make it compare more favorably to the data collected by a collimated source, meaning it could be more useful than the Zernike mode information. However, as seen previously, this additional error appears to not have a significant impact on the wind-on wavefront data collected with the FS-LIB spark, so removing it to collect data on the flowfield of interest may not be necessary in all cases.

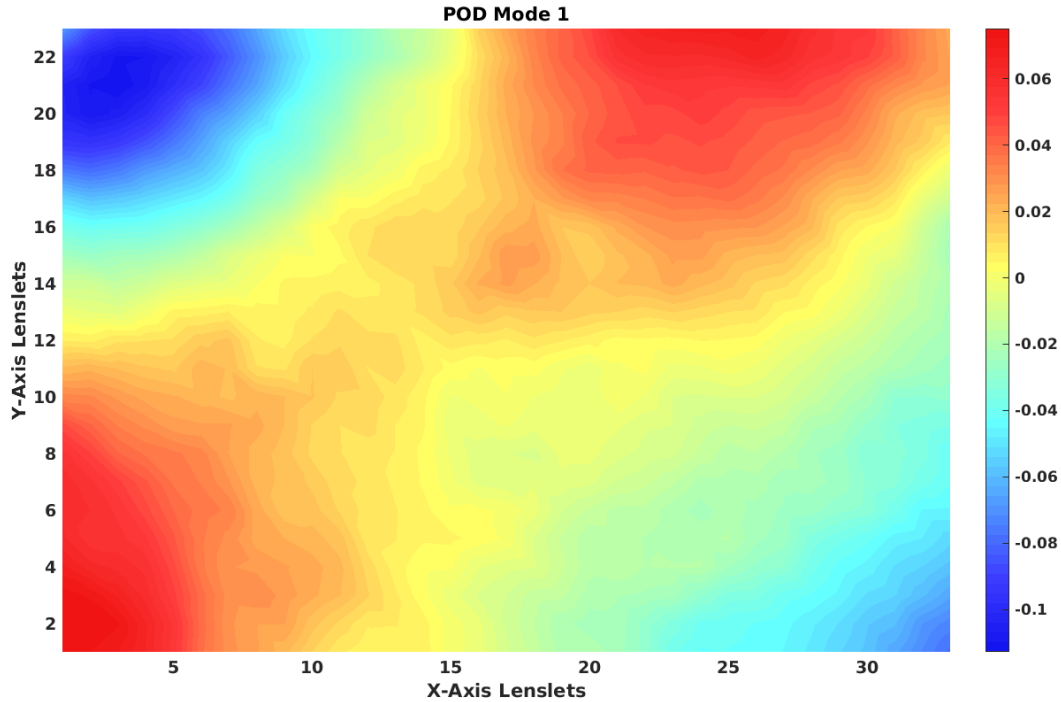


Figure 4.11: The most energetic POD mode for the FS-LIB Spark Wavefronts

#### 4.4 Comparisons to ND Model

Shown in this section is the comparison of the  $OPD_{rms}$  measured by the spark and the CW source to the model developed by the Notre Dame Aero-Optics group for a turbulent boundary layer. The Notre Dame model predicts, for a single boundary layer, an  $OPD_{rms}$  of approximately 12.8 nanometers. For two boundary layers, this number can be root-mean-squared added to itself, giving a total measureable distortion of approximately 18.2 nanometers[24]. Aperture effects must also be accounted for when using the Notre Dame model since the number it outputs assumes an infinite aperture size relative to the size of the boundary layer. Curves for the aperture size adjustment can be found in Lynch et. al.[11] for several Mach numbers. The final result is an  $OPD_{rms}$  of approximately 13 nanometers. A line indicating this value has been added to the

OPD<sub>rms</sub> time trace for the FS-LIB spark and is shown in Figure 4.12. The error bars on this trace come from propagating the error in the measurement of the supply and freestream conditions through to the model. As can be seen, this value is significantly below the actual measured OPD<sub>rms</sub> for the M3T’s boundary layers. However, the fact that both sources independently measured similar values for the boundary layer OPD<sub>rms</sub> suggests that this discrepancy does not stem solely from the FS-LIB spark introducing additional wavefront aberrations into the measurement. Rather, they likely come from additional factors in the experimental setup that were not accounted for. Possible sources of the increase in measured OPD<sub>rms</sub> could include tunnel vibration during the run or differences in the M3T’s boundary layers from the assumptions in the model.

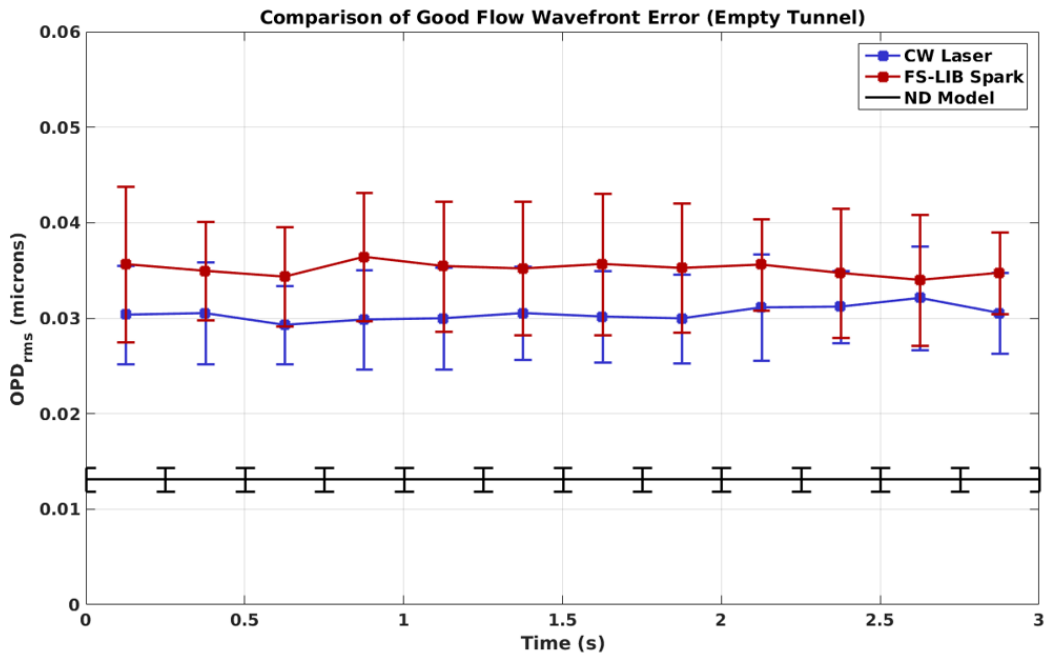


Figure 4.12: The CW Laser and FS-LIB Spark Source OPD<sub>rms</sub> compared to the Notre Dame Model

## Chapter 5: Conclusions and Future Work

### 5.1 Conclusions

The goal of this research was to determine if the FS-LIB spark can be used effectively as an aero-optic illumination source. Studying the behavior of a FS-LIB spark generated in air has indicated it is a promising illumination source for aero-optic measurements. Measurements of the FS-LIB spark in air show that the movement of the spark centroid is in the range of less than twenty microns for the experimental setup used in this work. This compares very favorably to nanosecond LIB spark behavior which previous work shows moves on the order of eighty to one hundred microns. In addition, the spark size and shape change are on the order of a few percent of the average size of the spark itself, which also corresponds to changes on the order of tens of microns. This means wavefront distortions introduced by changes in the spark's properties will be correspondingly much smaller, to the point where a tare wavefront capturing the mean spark-produced distortions could be sufficient to remove most of their effects without further processing. Additionally, in a lower-pressure environment, the FS-LIB spark becomes even more stable, with the centroid displacement decreasing to only a few microns pulse-to-pulse. It also begins to change shape in a lower-pressure environment, as FS laser-specific effects such as filamentation appear to become more present. This means wind-off tare images of the spark used for data reduction should be taken at the same pressure as that expected in the freestream of a

wind tunnel run for future applications.

Evidence of the spark's effectiveness as an aero-optic source was reinforced by the comparison of the wavefronts collected using the FS-LIB spark to wavefronts collected using a collimated laser source. The biggest difference in wavefront aberrations between the FS-LIB spark and the collimated laser source appeared when little or no flow was present. As the amount of flow-created wavefront aberrations increased, the measurements taken by the FS-LIB spark and the collimated laser agreed more closely, which indicated that the difference in measurement between the FS-LIB spark and the collimated laser are not directly coupled to flow disturbances. This means that as long as the flow-created aero-optic distortions are large enough relative to the wind-off noise from the spark, little or no additional post-processing may be necessary to extract meaningful data from measurements taken with a wavefront sensor. Additionally, the wavefront tilt introduced by the bulk motion of the spark correlated well to the spark centroid displacement. Tracking this with a second camera could therefore allow for accurate pulse-to-pulse removal of the spark-created tip and tilt if the flow-created tip and tilt was of interest for farfield data analysis. A series of modal analyses showed that the spark-created wavefront error was best captured through the use of proper orthogonal decomposition (POD), as the Zernike mode analysis showed that the spark error was spread over several low-order Zernike modes and not concentrated in a specific set. Both the spark data and collimated laser data were compared to an existing model for wavefront distortion developed by the Notre Dame Aero-Optics Group[9] and both (FS-LIB and collimated) sources showed discrepancies between the measured wavefront error and what is predicted by the model. However, this is likely due to an aspect of the M3T's behavior that differs from the assumptions made by the ND model, since both sources deviated from the model by nearly the same amount.

## 5.2 Future Work

The next step for evaluating the effectiveness of the FS-LIB spark is to test it in a larger facility, where the spark can be inserted into the flow and image a single wall boundary layer. As mentioned in Section 2, the small size of the M3T prevented the spark from being tested in this way for the present work. Evaluating the spark inside a moving flow would allow the study several new effects, such as how the motion of the spark with the flow and how the "stretching" and dimming of the spark at lower pressures would affect the wavefront data quality. Furthermore, using a facility that has already been used for aero-optic measurements and has been shown to compare well with theoretical models would allow for verification that the spark is not the cause of the discrepancy observed between the experimental wavefront data and the model's predictions as shown in this work.

Additionally, the effects of different focusing optics and laser power settings could be worth investigating. Work done previously on nanosecond LIB sparks have examined several focusing lens focal lengths and laser output power levels relative to the target gas breakdown threshold. Doing a similar analysis on the FS-LIB spark would help create a more complete comparison between the two sources, and it would also allow for further studying the effects of femtosecond laser-specific phenomena such as filamentation on the performance of the FS-LIB spark.

## Appendix A: MATLAB Code

Listing A.1: WFSReduceData.m

```
% Wavefront sensor image processing script
%
% Takes images acquired using a Shack-Hartmann WFS and calculates wavefront
% error
%
% Also does a bunch of post-processing analysis on the wavefronts
%
% -----

% Main

function wfs_reduce_data_thesis

cleanup;

% Load tare and run images
fprintf('Select folder for tare images.\n\n');
tareimgs = readimgs;
fprintf('Select folder for run images.\n\n');
runimgs = readimgs;
[tareimgs , runimgs] = wfsimadj(tareimgs ,runimgs);

% Processing start time
tv = tic;

% Generate subaperture from average tare image
tareavg = tareimgs{1};
for n = 2:length(tareimgs)
    tareavg = tareavg+tareimgs{n};
end
tareavg = tareavg ./ length(tareimgs);
[saptx ,spty ,J,K] = subap(tareavg);

% Pre-calculate sparse matrix inverse to save time
[E,P] = swmatgen(J,K);

% Save pre-processing time
tv1 = toc(tv);
```

```

% Calculate phase error and PSF for tare images
fprintf('Generating wavefronts ... ');
for n = 1:length(tareimgs)

    % Calculate final tare image centroids
    [xctare ,yctare ,~] = ctrds (tareimgs{n},saptx ,sapy ,J,K);

    % Calculate wavefront phase map
    wfetare{n} = fastswsvd(xctare ,yctare ,J,K,E,P);
    if rem(n,10) == 0
        fprintf(' ');
    end

end

% Calculate phase error and PSF for run images
for n = 1:length(runimgs)

    % Calculate final tare and run image centroids
    [xcrun ,ycrun ,~] = ctrds (runimgs{n},saptx ,sapy ,J,K);

    % Calculate wavefront phase map
    wferun{n} = fastswsvd(xcrun ,ycrun ,J,K,E,P);
    if rem(n,10) == 0
        fprintf(' ');
    end

end

fprintf(' \n\n ');

% Process wavefronts
[tareavg ,runavg ,rmtavg ,runinst] = wfavg(wferun ,wfetare);

% Generate a timescale to use as an x-axis
frate = 100; % Framerate (frames/sec)
taxis = scaletotime(frate ,numel(runimgs));

% Tip/tilt removal
[runinstrtt ,tiptilt ,ttcoeffs] = removetiptilt(runinst);

% Tip/tilt correlation
ttrun = input('Correlate tip/tilt to centroid movement? (1 == yes): ');
fprintf(' \n ');
if ttrun == 1
    ttcompare(ttcoeffs ,taxis);
end

% Calculate the OPDrms of each wavefront
opdrms = wfopdrms(runinstrtt);
fprintf('Average OPDrms of the instantaneous run wavefronts (tip/tilt removed): %

% Plot OPDrms time trace

```

```

figure;
plot(taxis ,opdrms , 'Linewidth' ,1.5);
title ('Time Trace of OPD_r_m_s');
xlabel ('Time (s)');
ylabel ('OPD_r_m_s (microns)');

% Moving average
npavg = 25;
[movavgopdrms ,opde] = variavg(opdrms ,npavg);

% Plot moving average and standard deviation
figure;
errorbar(movavgopdrms ,opde , 's' , 'Color' ,[1 0 0.5] , 'Linewidth' ,1.5 , ...
    'MarkerSize' ,8);
title ('Moving Average of OPD_r_m_s');
xlabel ('Averaged Set');
ylabel ('OPD_r_m_s (microns)');
eline = findobj(gcf , 'type' , 'errorbar');

% Combine previous two plots
figure;
plot(taxis ,opdrms , 'LineWidth' ,1.0);
hold on;
errorbar(eline.XData*(npavg/frate) ,eline.YData ,eline.UData , ...
    's' , 'Color' ,[1 0.5 0] , 'LineWidth' ,1.5 , 'MarkerSize' ,8);
title ('Comparison of Raw OPD_r_m_s Trace to Moving Average');
xlim([0 taxis(end)]);
xlabel ('Time (s)');
ylabel ('OPD_r_m_s (microns)');
hold off;

% Zernike mode decomposition
[wfzs , wfzcs] = wfzernike(runinstrtt);

% Do a POD analysis
wfpodmodes = wfpod(runinstrtt);

fprintf ('Wavefront generation time: %5.3f seconds\n\n' ,toc(tv)-tv1);

% Generate a bunch of plots of the data
makeplots(tareavg ,runavg ,rmtavg ,runinst ,runinstrtt);

close all;

fprintf ('Total WFS data reduction time: %5.3f seconds\n\n' ,toc(tv));

end

% -----

% Image Read Function

function imgs = readimgs()

```

```

% Search in folders using GUI
pathname = uigetdir('~/Documents/Aero_Optics/');
fprintf('Loading images...\n\n');
imgdir = dir(strcat(pathname));
nimgs = length(imgdir);
for i = 3:nimgs
    imgs{i-2} = im2double(imread(strcat(pathname, '/' ,imgdir(i).name)));
    % Dump extra array dimensions if present
    if ndims(imgs{i-2}) > 2
        imgs{i-2}(:, :, 4) = [];
        imgs{i-2} = rgb2gray(imgs{i-2});
    end
end

% Transpose input (will make all future calculations make more sense)
for n = 1:length(imgs)
    imgs{n} = imgs{n}';
end

end

% -----

% Image adjustment

function [tareadj,runadj] = wfsimadj(tareimgs,runimgs)

% Open the first image in the cropping tool
fprintf(['Use the cursor to place the cropping rectangle. '...
    'Double-click to finish.\n\n']);
tuneimg = imadjust(tareimgs{1},[0 0.4],[]);
[~,resz] = imcrop(tuneimg);

% Apply adjustment to all remaining images
fprintf('Applying adjustment to remaining images...\n\n');
for n = 1:length(tareimgs)
    tareadj{n} = imcrop(tareimgs{n},[],resz);
    tareadj{n}(1:10,1:end) = 0; tareadj{n}(end-10:end,1:end) = 0;
    tareadj{n}(1:end,1:10) = 0; tareadj{n}(1:end,end-10:end) = 0;
    tareadj{n} = padarray(tareadj{n},[50 50], 'both');
end

for n = 1:length(runimgs)
    runadj{n} = imcrop(runimgs{n},[],resz);
    runadj{n}(1:10,1:end) = 0; runadj{n}(end-10:end,1:end) = 0;
    runadj{n}(1:end,1:10) = 0; runadj{n}(1:end,end-10:end) = 0;
    runadj{n} = padarray(runadj{n},[50 50], 'both');
end

fprintf('Image adjustment complete.\n\n');

close all

```

**end**

% -----

*% Subaperture Calculator Function*

**function** [s\_x , s\_y , J , K] = subap(img)

*% Tunable parameters*

spacing = 50; *% Pixels between centroids*

*% Source centroid generation for subapertures*

*%Image Adjustment*

imfilt = imgaussfilt(img,1);

imadj = imfilt/**max**(**max**(imfilt));

imadj = imadjust(imadjust(imadj),[0.2 0.7],[[]]);

imbw = im2bw(imadj);

*% Centroid location generation*

cts = regionprops(imbw, 'Centroid');

cts = cat(1, cts.Centroid);

cx = cts(:,1); cy = cts(:,2);

*% Subaperture generation*

*% Number of points in each direction*

J = **round**((**max**(cx)-**min**(cx))/spacing)+1;

K = **round**((**max**(cy)-**min**(cy))/spacing)+1;

*% Figuring out where the center point is (or closest to center)*

**if** **rem**(J,2) == 0

    cpx = **round**((**max**(cx)+**min**(cx))/2) - spacing);

**else**

    cpx = **round**((**max**(cx)+**min**(cx))/2) - spacing/2);

**end**

**if** **rem**(K,2) == 0

    cpy = **round**((**max**(cy)+**min**(cy))/2) - spacing);

**else**

    cpy = **round**((**max**(cy)+**min**(cy))/2) - spacing/2);

**end**

*% Define location to start generating subapertures from (top-left)*

xedge = **ceil**(J/2);

yedge = **ceil**(K/2);

*% Defining top-left corners of subaperture regions*

**for** i = 1:J

**for** j = 1:K

        Bx(i,j) = (cpx+(i-xedge)\*spacing);

        By(i,j) = (cpy+(j-yedge)\*spacing);

```
end  
end
```

```
% Output subaperture values  
s_x = Bx;  
s_y = By;
```

```
end
```

```
% -----
```

```
% Centroid Location Function
```

```
function [xc,yc,I] = ctrds(img,s_x,s_y,J,K)
```

```
% First-moment centroid calculation with gamma correction  
% Original reference: Nightingale and Gordeyev
```

```
% Tunable Parameters
```

```
gamma = 4; % Order of gamma correction  
threshold = 0.2; % Image minimum intensity threshold  
spacing = 50;
```

```
% Centroid calculation
```

```
% Load in all of our necessary information
```

```
Bx = s_x;  
By = s_y;
```

```
% % First-moment centroid with gamma correction and thresholding
```

```
for i = 1:J
```

```
    for j = 1:K
```

```
        b = img(By(i,j):By(i,j)+spacing ,...  
                Bx(i,j):Bx(i,j)+spacing );
```

```
        bnorm = b./max(max(b));
```

```
        bgamma = bnorm.^gamma;
```

```
        bgamma = bgamma-threshold*max(max(bgamma));
```

```
        bgamma(bgamma<0) = 0;
```

```
        sumx = 0;sumy = 0;sum = 0;
```

```
        for k = 1: numel(b(:,1))
```

```
            for l = 1: numel(b(1,:))
```

```
                sumx = sumx+l*bgamma(k,l);
```

```
                sumy = sumy+k*bgamma(k,l);
```

```
                sum = sum+bgamma(k,l);
```

```
            end
```

```
        end
```

```
% Centroids for each subaperture as well as the intensity sum
```

```
xc(i,j) = sumx/sum-1;
```

```
yc(i,j) = sumy/sum-1;
```

```

        I(i,j) = sum;

        % Test centroids moved by spacing values for plotting
        xcpl(i,j) = xc(i,j)+Bx(i,j);
        ycpl(i,j) = yc(i,j)+By(i,j);

    end
end

end

% -----

% Generator of Existence and Phase Matrices (Only Called Once)
function [E,P] = swmatgen(J,K)

% Existence matrix
E = ones(J+2,K+2);
E(1,:) = 0; E(end,:) = 0; E(:,1) = 0; E(:,end) = 0;

% Phase equation matrix
P = zeros(J*K,J*K);
for j = 1:J
    for k = 1:K
        P((j-1)*K+k,(j-1)*K+k) = E(j,k+1)+E(j+2,k+1)+E(j+1,k)+E(j+1,k+2);
        if E(j,k+1) == 1
            P((j-1)*K+k,(j-2)*K+k) = -1;
        end
        if E(j+2,k+1) == 1
            P((j-1)*K+k,(j)*K+k) = -1;
        end
        if E(j+1,k) == 1
            P((j-1)*K+k,(j-1)*K+(k-1)) = -1;
        end
        if E(j+1,k+2) == 1
            P((j-1)*K+k,(j-1)*K+(k+1)) = -1;
        end
    end
end

end

% Invert phase matrix (only need to do once!)
P = pinv(P);

end

% -----

% Fast Southwell Method (Direct Inversion w/ Quick Matrix Gen)
function wfe = fastswsvd(xc,yc,J,K,E,P)

% WFS parameters (to produce results in engineering units)
spacing = 50;
pixsz = 11;

```

```

f1 = 44000;

% Far-field angle calculation (relies on small-angle approximation)
for i = 1:J
    for j = 1:K
        thetax(i,j) = (xc(i,j)-spacing/2)*(pixsz/f1);
        thetay(i,j) = (yc(i,j)-spacing/2)*(pixsz/f1);
    end
end

% Height of subregion in pixels
h = pixsz*spacing;

% Slope vector
S = zeros(J*K);
for j = 1:J
    for k = 1:K
        if E(j,k+1) == 1
            S((j-1)*K+k) = S((j-1)*K+k)+(h/2)*thetax(j-1,k);
        end
        if E(j+2,k+1) == 1
            S((j-1)*K+k) = S((j-1)*K+k)-(h/2)*thetax(j+1,k);
        end
        if E(j+1,k) == 1
            S((j-1)*K+k) = S((j-1)*K+k)+(h/2)*thetay(j,k-1);
        end
        if E(j+1,k+2) == 1
            S((j-1)*K+k) = S((j-1)*K+k)-(h/2)*thetay(j,k+1);
        end
    end
end

% Invert to solve for phase
w = P*S;

% Re-organize back into a matrix
wfe = zeros(J,K);
for j = 1:J
    for k = 1:K
        wfe(j,k) = w((j-1)*K+k);
    end
end

% -----

% Image Averaging and Tare Subtraction

function [tareavg ,runavg ,rmtavg ,runinst] = wfavg(wferun ,wfetare)

% Generate average tare wavefront
tareavg = wfetare{1};

```

```

for n = 2:length(wfetare)
    tareavg = tareavg + wfetare{n};
end
tareavg = tareavg/length(wfetare);

% Generate average run wavefront
runavg = wferun{1};
for n = 2:length(wferun)
    runavg = runavg + wferun{n};
end
runavg = runavg/length(wferun);

% Subtract average tare wavefront from average run wavefront
rmtavg = runavg-tareavg;

% Subtract mean run image to non-instantaneous information
for j = 1:length(wferun)
    runinst{j} = wferun{j}-tareavg;
end

end

% -----

% Tip/Tilt Removal

function [adjwfs ,tts ,ttcoeff] = removetiplt(wfs)

% Figure out dimensions of wavefront in terms of grid
J = numel(wfs{1}(:,1)); K = numel(wfs{1}(1,:));

for n = 1:length(wfs)
    % Generate plane fit of each wavefront
    for j = 1:J
        for k = 1:K
            x((j-1)*K+k) = j;
            y((j-1)*K+k) = k;
            z((j-1)*K+k) = wfs{n}(j,k);
        end
    end
    c = ones(size(x));
    pfit = [x' y' c']\z';
    pfitx = pfit(1);
    pfity = pfit(2);
    pfitc = pfit(3);

    % Construct plane with coefficients
    for j = 1:J
        for k = 1:K
            tt(j,k) = pfitx*x((j-1)*K+k)+pfity*y((j-1)*K+k)+pfitc;
        end
    end

```

```

% Output adjusted wavefronts
adjwfs{n} = wfs{n}-tt;

% Output tip/tilt plane (for plotting)
tts{n} = tt;

% Output coefficients in an array
ttcoeff(n,:) = [pfitx pfity pfitc];

end

end

% -----

% Tip/Tilt Comparison to Centroid Shift

function ttcompare(ttcoeffs ,taxis)

% Define a scaling factor for pixels to um (hard-coded for now)
sf = 25.1031/1000;

% Run spark analyzer code to get centroid movement
SparkAnalyzer_v2_mod

% Break out vectors
shift = cell2mat(delcen')/sf;
% Camera reads in pre-trigger images backwards for some reason
ctdata = input('Wind-off data? (1 == yes): ');
fprintf('\\n');
if ctdata == 1
    shift = flip(shift);
end
xshift = shift(:,1); yshift = shift(:,2);
% Note: tip and tilt scaled by two to convert the slopes to mrad (1e3/500)
tip = 2*ttcoeffs(:,2); tilt = 2*ttcoeffs(:,1);

% Calculate Linear Regression Coefficients
tipfit = polyfit(xshift ,tip ,1);
tiltfit = polyfit(yshift ,tilt ,1);

% Calculate R^2 values
tipest = polyval(tipfit ,xshift);
SStip = sum((tip-tipest).^2);
SStiptot = (length(tip)-1)*var(tip);
R2tip = 1-SStip/SStiptot;
tiltest = polyval(tiltfit ,yshift);
SStilt = sum((tilt-tiltest).^2);
SStilttot = (length(tilt)-1)*var(tilt);
R2tilt = 1-SStilt/SStilttot;

% Print fit curves and R^2 values to console
fprintf('Tip/X-Shift fit line: y = %6.4fx + %6.4f\\n\\n',tipfit(1),tipfit(2));

```

```

fprintf('Tip/X-Shift R^2 value: %6.4f\n\n',R2tip);
fprintf('Tilt/Y-Shift fit line: y = %6.4fx + %6.4f\n\n',tiltfit(1),tiltfit(2));
fprintf('Tilt/Y-Shift R^2 value: %6.4f\n\n',R2tilt);

```

```

% Plot of tip and tilt traces

```

```

figure;
plot(taxis ,tip -mean(tip) , 'Color' ,[0.2 0.2 0.8] , 'LineWidth' ,1.5);
hold on;
plot(taxis ,tilt -mean(tilt) , 'Color' ,[0.8 0.2 0.2] , 'LineWidth' ,1.5);
title('Time Traces of Wavefront Tip and Tilt (Mean-Subtracted)');
xlabel('Time (s)');
ylabel('Tip/Tilt (mrad)');
legend('Tip' , 'Tilt');
hold off;

```

```

% Plot of tip to x-shift correlation

```

```

figure;
plot(xshift ,tip , 'o' , 'Color' ,[0 0.75 0.5] , 'MarkerFaceColor' ,[0 0.75 0.5]);
hold on
plot(xshift ,tipest , 'k' , 'Linewidth' ,1.5);
text(max(xshift)/4 ,max(tip)/4 ,...
    ['R^2 = ' ,num2str(R2tip)] , 'FontSize' ,14 , 'FontWeight' , 'bold');
title('Tip/X-Shift Correlation');
xlabel('Centroid x-shift (microns)');
ylabel('Tip (mrad)');

```

```

hold off

```

```

% Plot of tilt to y-shift correlation

```

```

figure;
plot(yshift ,tilt , 'o' , 'Color' ,[0.5 0 0.75] , 'MarkerFaceColor' ,[0.5 0 0.75]);
hold on
plot(yshift ,tiltest , 'k' , 'Linewidth' ,1.5);
text(max(yshift)/4 ,max(tilt)/4 ,...
    ['R^2 = ' ,num2str(R2tilt)] , 'FontSize' ,14 , 'FontWeight' , 'bold');
title('Tilt/Y-Shift Correlation');
xlabel('Centroid y-shift (microns)');
ylabel('Tilt (mrad)');
legend('Test Data' , 'Fit Line');
hold off

```

```

end

```

```

% -----

```

```

% Calculate Optical Path Difference

```

```

function opd rms = wfopdrms(wfs)

```

```

% OPDrms for instantaneous run images

```

```

for n = 1:length(wfs)
    rwf = wfs{n};

```

```

    opdtemp = 0;
    for j = 1:numel(rwf(:,1))
        for k = 1:numel(rwf(1,:))
            opdtemp = opdtemp + (rwf(j,k)^2);
        end
    end
    end
    % RMS calculation
    opdrms(n) = sqrt(opdtemp/numel(rwf));
    clear rwf;
end
end

```

% -----

*% Moving Average Calculator*

```

function [traceout ,e] = variavg(tracein ,npavg)

for n = 1:(length(tracein)/npavg)
    wdw = tracein((n-1)*npavg+1:n*npavg);
    e(n) = 2*std(wdw);
    traceout(n) = mean(wdw);
end

end

```

% -----

*% Zernike Mode Decomposition (Using Noll's Notation)*

```

function [wfmodes ,wfmcoeffs] = wfmzernike(wfs)

```

*% Define our grid*

```

JK = [numel(wfs{1}(:,1)) numel(wfs{1}(1,:))];
R = floor(min(JK)/2);
jkdifff = abs(JK(1)-JK(2))/2;

```

*% Build our Zernike mode matrix*

```

Z= [];
for j = 1:JK(1)
    for k = 1:JK(2)
        r = sqrt((j-R-1)^2+(k-R-jkdifff-1)^2);
        th = atan2((k-R-jkdifff-1),(j-R-1));
        if r <= R
            r = r/R;
            Z((j-1)*JK(2)+k,:) = [1 2*r*cos(th) 2*r*sin(th) sqrt(3)*(2*r^2-1) ...
                sqrt(6)*(r^2)*sin(2*th) sqrt(6)*(r^2)*cos(2*th) ...
                sqrt(8)*(3*r^3-2*r)*sin(th) sqrt(8)*(3*r^3-2*r)*cos(th) ...
                sqrt(8)*(r^3)*sin(3*th) sqrt(8)*(r^3)*cos(3*th) ...
                sqrt(5)*(6*r^4-6*r^2+1) ...
                sqrt(10)*(4*r^4-3*r^2)*cos(2*th) sqrt(10)*(4*r^4-3*r^2)*sin(2*th)
                sqrt(10)*(r^4)*cos(4*th) sqrt(10)*(r^4)*sin(4*th) ...

```

```

        sqrt(12)*(10*r^5-12*r^3+3*r)*cos(th) sqrt(12)*(10*r^5-12*r^3+3*r)*
        sqrt(12)*(5*r^5-4*r^3)*cos(3*th) sqrt(12)*(5*r^5-4*r^3)*sin(3*th)
        sqrt(12)*(r^5)*cos(5*th) sqrt(12)*(r^5)*sin(5*th)]';
    else
        Z((j-1)*JK(2)+k,:) = zeros(21,1);
    end
end
end
for n = 1:numel(wfs)

    % Create wavefront vector
    for j = 1:JK(1)
        for k = 1:JK(2)
            r = sqrt((j-R-1)^2+(k-R-jkdiff-1)^2);
            if r <= R
                wf((j-1)*JK(2)+k) = wfs{n}(j,k);
            else
                wf((j-1)*JK(2)+k) = 0;
            end
        end
    end

    % Perform least squares fit
    a = Z\wf';

    size(a);

    % Output coefficients for each image
    wfzcoeffs{n} = a;

    % Reconstruct modes and output
    zvec = Z*a;
    for j = 1:JK(1)
        for k = 1:JK(2)
            wfzmode(j,k) = zvec((j-1)*JK(2)+k);
        end
    end

    % Save modes (if viewing them later is desired)
    wfzmodes{n} = wfzmode;

end

% Generate average coefficient values through a whole run
avgzc = abs(wfzcoeffs{1});
for n = 2:numel(wfzcoeffs);
    avgzc = avgzc+abs(wfzcoeffs{n});
end
avgzc = avgzc/numel(wfzcoeffs);
maxzcavg = max(avgzc);

% Plot averaged coefficients

```

```

figure;
plot(avgzc, 'Linewidth', 1.5)
grid on;
xlim([1 21]);
title('Contribution of First Twenty-One Zernike Modes');
xlabel('Zernike Mode');
ylabel('Contribution');

% Plot normalized averaged coefficients
figure;
plot(avgzc/maxzcavg, 'Linewidth', 1.5, 'Color', [0.8 0.2 0.2])
grid on;
xlim([1 21]);
title('Contribution of First Twenty-One Zernike Modes (Normalized)');
xlabel('Zernike Mode');
ylabel('Contribution');

% Test removal of Zernike modes
zsubwf = wfs{round(end/2)} - wfzmodes{round(end/2)};

% Plot the modal reconstruction
figure;
surf(wfzmodes{round(end/2)});
view([45 60]);
xlabel('X-Axis Lenslets');
ylabel('Y-Axis Lenslets');
zlabel('OPD');
title('Zernike Mode Map Reconstruction');

% Plot the modal reconstruction removed from the wavefront
figure;
surf(wfs{round(end/2)} - wfzmodes{round(end/2)});
view([45 60]);
xlabel('X-Axis Lenslets');
ylabel('Y-Axis Lenslets');
zlabel('OPD');
title('Check to See Accuracy of Zernike Mode Reconstruction');

end

% -----

% POD Analysis

function wfpodmodes = wfpod(wfs)

% Define our grid
J = numel(wfs{1}(:,1));
K = numel(wfs{1}(1,:));

% Construct the concatenated matrix of WF data
for n = 1:numel(wfs)

```

```

    wf = wfs{n};
    for j = 1:J
        for k = 1:K
            U(n,(j-1)*K+k) = wf(j,k);
        end
    end
end

% Covariance matrix
C = (1/(numel(wfs)-1))*(U'*U);

% POD Modes (Eigenvectors)
[phi,e] = eig(C,'vector');

% Reconstruct wavefronts from POD modes
phiout = {};
for n = 1:numel(phi(1,:))
    for j = 1:J
        for k = 1:K
            phiwfe(j,k) = phi((j-1)*K+k,n);
        end
    end
    phiout{n} = phiwfe;
end

% Plot highest-energy POD mode
figure;
surf(phiout{end});
view([45 60]);
xlabel('X-Axis Lenslets');
ylabel('Y-Axis Lenslets');
zlabel('OPD_r.m.s');
title('POD Mode 1');

% Calculate OPDrms of POD modes (scaled by contribution)
for n = 1:numel(phiout)
    wfpodmodes{n} = e(n)*phiout{n};
end
phiopd = wfopdrms(wfpodmodes);
fprintf('Average OPDrms of all POD modes: %7.5f um \n\n',mean(phiopd));

% Plot eigenvalues
figure;
plot(e(end:-1:end-9),'Linewidth',1.5);
title('First Ten POD Modes');
xlabel('POD Mode');
ylabel('Contribution');

% Plot OPDrms
figure;
plot(phiopd,'Linewidth',1.5);
xlabel('POD Mode');
ylabel('OPD_r.m.s (microns)');

```

**end**

*% -----*

*% Time axis generator*

**function** taxis = scaletotime(frate , numimgs)

taxis = (1/frate):(1/frate):(numimgs/frate);

**end**

*% -----*

*% Generate a bunch of surface plots*

**function** makeplots(tareavg , runavg , rmtavg , runinst , runinsttt)

**figure**;

**surf**(tareavg);

**view**([45 60]);

**xlabel**('X-Axis Lenslets');

**ylabel**('Y-Axis Lenslets');

**zlabel**('OPD');

**title**('Average Tare Wavefront');

**figure**;

**surf**(runavg);

**view**([45 60]);

**xlabel**('X-Axis Lenslets');

**ylabel**('Y-Axis Lenslets');

**zlabel**('OPD');

**title**('Average Run Wavefront');

**figure**;

**surf**(rmtavg);

**view**([45 60]);

**xlabel**('X-Axis Lenslets');

**ylabel**('Y-Axis Lenslets');

**zlabel**('OPD');

**title**('Average Tare-Subtracted Wavefront Error');

**figure**;

**surf**(runinst{**round**(end/2)});

**view**([45 60]);

**xlabel**('X-Axis Lenslets');

**ylabel**('Y-Axis Lenslets');

**zlabel**('OPD');

**title**('Instantaneous Mean-Subtracted Wavefront Error');

**figure**;

**surf**(runinst{**round**(end/2)});

```

view([0 90]);
xlabel('X-Axis Lenslets ');
ylabel('Y-Axis Lenslets ');
zlabel('OPD');
title('Instantaneous Mean-Subtracted Wavefront Error');

figure;
surf(runinstrtt{round(end/2)});
view([45 60]);
xlabel('X-Axis Lenslets ');
ylabel('Y-Axis Lenslets ');
zlabel('OPD');
title('Instantaneous Mean-Subtracted Wavefront Error (Tip/Tilt Removed)');

figure;
surf(runinstrtt{round(end/2)});
view([0 90]);
xlabel('X-Axis Lenslets ');
ylabel('Y-Axis Lenslets ');
zlabel('OPD');
title('Instantaneous Mean-Subtracted Wavefront Error (Tip/Tilt Removed)');

% Fast-format all figures
quickfigureformatter
pause();

end

% -----

% Clean-Up Function

function cleanup

close all;
clear;
clc;

end

```

## Listing A.2: SparkAnalyzerV2.m

```

% Raw Spark Image Processor v2.0

% Updated FS-LIB spark analysis code that calculates deviation in size and
% shape from the mean in order to compare to changes in wavefront phase

% -----

% Clear everything that is currently open
close all
clear
clc
% Start a timer
tv = tic;
fprintf('Initializing spark analysis...\n\n')

%% Image Importation

% Bring raw images in from folders

% Use GUI to navigate to desired folder
pathname = uigetdir('~/Documents/Aero_Optics/');
fprintf('Loading images...\n\n');
imgdir = dir(strcat(pathname));
nimgs = length(imgdir);
for i = 3:nimgs
    imgs{i-2} = im2double(imread(strcat(pathname, '/' ,imgdir(i).name)));
    % Dump extra array dimensions if present (want greyscale images)
    if ndims(imgs{i-2}) > 2
        imgs{i-2}(:, :, 4) = [];
        imgs{i-2} = rgb2gray(imgs{i-2});
    end
end

% Time check
et = toc(tv);
fprintf('Time to read images: %5.3f seconds\n\n', et)

%% Mean Image Generation

% Create a mean image from all of the images in a folder

fprintf('Generating mean images...\n\n');

meaning = imgs{1};
for i = 2:length(imgs)
    meaning = meaning + imgs{i};
end
meaning = meaning/numel(imgs);
figure;
imshow(meaning, []);

%% Image Processing

```

```
% Performing several steps of image processing to convert the mean image  
% to a black-and-white plot of the spark
```

```
fprintf('Processing images...\n\n');  
imfilt = meanimg;  
adjspark = imfilt.^2; % Gamma correction  
lv = graythresh(adjspark);  
bwspark = im2bw(adjspark,lv);
```

```
%% Mean Spark Image Analysis
```

```
% Generate mean values to be referenced in later steps
```

```
% Calculate the size of the spark in pixels
```

```
global sparkstats;  
pixtodim = 25.1031; % Conversion factor (pixels/mm)  
%pixtodim = 33.3655; % Use this value for vacuum cell data  
centroids = {};  
bwspark = double(bwspark);  
% Extract the desired spark dimensions  
sparkprops = regionprops(bwspark, 'centroid', 'Area', ...  
    'MajorAxisLength', 'MinorAxisLength', 'Extrema');  
ct = cat(1, sparkprops.Centroid);  
sparkwidth = sparkprops.MinorAxisLength;  
sparkheight = sparkprops.MajorAxisLength;  
sparkarea = sparkprops.Area;  
sparkextent = sparkprops.Extrema;  
sparkstats.width = sparkwidth;  
sparkstats.height = sparkheight;  
sparkstats.area = sparkarea;  
sparkstats.centroid = ct;  
sparkstats.extrema = sparkextent;  
centroids = ct';  
% Print out mean values  
fprintf('Spark Width: %7.5f mm\n\n', sparkwidth/pixtodim);  
fprintf('Spark Height: %7.5f mm\n\n', sparkheight/pixtodim);  
fprintf('Spark Area: %7.5f mm^2\n\n', sparkarea/(pixtodim^2));
```

```
%% Calculate Differences from Mean
```

```
% All mean-subtracted values are generated here and converted to EU
```

```
% Import the mean values
```

```
refimg = meanimg;  
refcen = sparkstats.centroid;  
refarea = sparkstats.area;  
refheight = sparkstats.height;  
refwidth = sparkstats.width;  
delcen = {};
```

```
% Set up loop to run through each image
```

```
for i = 1:numel(imgs)
```

```

origimg = imgs{i};
origadj = origimg.^2;
origlv = graythresh(origadj);
origbw = im2bw(origadj, origlv);
origstats = regionprops(origbw, 'centroid', 'area', ...
    'majoraxislength', 'minoraxislength');
origsz = cat(1, origstats.Area);
origght = cat(1, origstats.MajorAxisLength);
origwdh = cat(1, origstats.MinorAxisLength);
origct = cat(1, origstats.Centroid);
sdist = 9999;
% Figure out which object in view is the spark
% Added because occasionally dust particles pass through camera view
if length(origsz) > 1
    spkarea = max(origsz);
    spkheight = max(origght);
    spkwidth = max(origwdh);
    for k = 1:length(origsz)
        cenloc(k) = sqrt(((origct(k,1)-refcen(1))^2) + ((origct(k,2)-refcen(2)
    end
    [~,oi] = min(cenloc);
else
    spkarea = origsz;
    spkheight = origght;
    spkwidth = origwdh;
    oi = 1;
end
clear cenloc;

% Calculate delta values
origct = [origct(oi,1) origct(oi,2)];
delct = origct-refcen;
spkhgts{i} = spkheight;
delhgt{i} = spkheight-refheight;
delhgtpcnt{i} = ((spkheight-refheight)/refheight)*100;
delwdhpcnt{i} = ((spkwidth-refwidth)/refwidth)*100;
delwdh{i} = spkwidth-refwidth;
spkwtdts{i} = spkwidth;
spkareas{i} = spkarea;
delsz{i} = spkarea-refarea;
delszpcnt{i} = ((spkarea-refarea)/refarea)*100;
delcen{i} = delct;
end

% Calculate norm of centroid shift
cendist = {};
for i = 1:length(delcen)
    cendist{i} = norm(delcen{i});
end

% These are used by the mod code for comparison to WF data
delmat = cell2mat(delcen');
xcshift = delmat(:,1);

```

```

ycshift = delmat(:,2);
maxdev = max(cell2mat(cendist));
avgdev = mean(cell2mat(cendist));

% Print out a bunch of values to be tabulated
fprintf('Spark Width STDev: %7.5f mm\n\n',std(cell2mat(spkwtdts))/pixtodim);
fprintf('Spark Height STDev: %7.5f mm\n\n',std(cell2mat(spkhgts))/pixtodim);
fprintf('Spark Area STDev: %7.5f mm\n\n',std(cell2mat(spkareas))/(pixtodim^2));
fprintf('Spark Centroid Shift (Norm): Average = %7.5f microns, STD = %7.5f microns\n\n',
mean(cell2mat(cendist)*(1000/pixtodim)),std(cell2mat(cendist)*(1000/pixtodim)));
fprintf('Spark Centroid X-Shift: Average = %7.5f microns, STD = %7.5f microns\n\n',
mean(abs(xcshift)*(1000/pixtodim)),std(abs(xcshift)*(1000/pixtodim)));
fprintf('Spark Centroid Y-Shift: Average = %7.5f microns, STD = %7.5f microns\n\n',
mean(abs(ycshift)*(1000/pixtodim)),std(abs(ycshift)*(1000/pixtodim)));
fprintf('Spark Area Change: Average = %7.5f mm^2, STD = %7.5f mm^2\n\n',...
mean(abs(cell2mat(delszpcent)))/(pixtodim^2),std(abs(cell2mat(delszpcent)))/(pixtodim^2));
fprintf('Spark Width Change: Average = %7.5f mm, STD = %7.5f mm\n\n',...
mean(abs(cell2mat(delwdhpcnt))/pixtodim),std(abs(cell2mat(delwdhpcnt))/pixtodim));
fprintf('Spark Height Change: Average = %7.5f mm, STD = %7.5f mm\n\n',...
mean(abs(cell2mat(delhgtpcnt))/pixtodim),std(abs(cell2mat(delhgtpcnt))/pixtodim));
fprintf('Spark Percent Area Change: Average = %7.5f percent, STD = %7.5f percent\n\n',...
mean(abs(cell2mat(delszpcent))),std(abs(cell2mat(delszpcent))));
fprintf('Spark Percent Width Change: Average = %7.5f percent, STD = %7.5f percent\n\n',...
mean(abs(cell2mat(delwdhpcnt))),std(abs(cell2mat(delwdhpcnt))));
fprintf('Spark Percent Height Change: Average = %7.5f percent, STD = %7.5f percent\n\n',...
mean(abs(cell2mat(delhgtpcnt))),std(abs(cell2mat(delhgtpcnt))));

%% Plot Generation

fprintf('Generating plots...\n\n');

% Convert x-axis to time
imct = numel(imgs);
framerate = 100; % Frames/sec
taxis = (1/framerate):(1/framerate):(imct/framerate);

% Plot of centroid movement in pix
figure;
plot(taxis,cell2mat(cendist),'o','Color',[0 0 1],...
'MarkerFaceColor',[0 0 1],'MarkerSize',5);
% ylim([0 4]);
title('Centroid Shift of Spark from Mean');
xlabel('Time (s)');
ylabel('Centroid Shift (pixels)');
legend('Image');

% Plot of centroid movement in mm
figure;
plot(taxis,cell2mat(cendist)/pixtodim,'o','Color',[0 0 1],...
'MarkerFaceColor',[0 0 1],'MarkerSize',5);
% ylim([0 0.1]);
title('Centroid Shift of Spark from Mean');
xlabel('Time (s)');

```

```

ylabel('Centroid Shift (mm)');
legend('Image');

% Plot of centroid movement in microns
figure;
plot(taxis ,cell2mat(cendist)/(pixtodim/1000),'o','Color',[0 0 1],...
    'MarkerFaceColor',[0 0 1],'MarkerSize',5);
% ylim([0 100]);
title('Centroid Shift of Spark from Mean');
xlabel('Time (s)');
ylabel('Centroid Shift (microns)');
legend('Image');

% Centroid y-movement plotted against centroid x-movement
figure;
plot((xcshift*(1000/pixtodim)),(ycshift*(1000/pixtodim)),'o',...
    'Color',[0 0 0.8],'MarkerFaceColor',[0 0 0.8])
axis equal;
title('Centroid Shift of Spark from Mean');
xlabel('X-Shift (Microns)');
ylabel('Y-Shift (microns)');
legend('Image');

% Plot of area change
figure;
plot(taxis ,cell2mat(delsz),'o','Color',[0.9 0 0],...
    'MarkerFaceColor',[0.9 0 0],'MarkerSize',5);
title('Change in Spark Area from Mean Image');
xlabel('Time (s)');
ylabel('Area Change (pixels)');
legend('Image');

% Plot of percent area change
figure;
plot(taxis ,cell2mat(delszpcnt),'o','Color',[0 0.8 0],...
    'MarkerFaceColor',[0 0.8 0],'MarkerSize',5);
title('Change in Spark Area from Mean Image');
xlabel('Time (s)');
ylabel('Percent Area Change');
legend('Image');

% Plot of width change
figure;
plot(taxis ,cell2mat(delwdh)*(1000/pixtodim),'o','Color',[0.5 0 0.75],...
    'MarkerFaceColor',[0.5 0 0.75],'MarkerSize',5);
title('Change in Spark Width from Mean Image');
xlabel('Time (s)');
ylabel('Width Change (microns)');
legend('Image');

% Plot of height change
figure;
plot(taxis ,cell2mat(delhgt)*(1000/pixtodim),'o','Color',[0.75 0 0.5],...

```

```

    'MarkerFaceColor',[0.75 0 0.5], 'MarkerSize',5);
title('Change in Spark Height from Mean Image');
xlabel('Time (s)');
ylabel('Height Change (microns)');
legend('Image');

% Plot of percent width change
figure;
plot(taxis , cell2mat(delwdhpcnt), 'o', 'Color',[0 0.5 0.75],...
    'MarkerFaceColor',[0 0.5 0.75], 'MarkerSize',5);
title('Percent Change in Spark Width from Mean Image');
xlabel('Time (s)');
ylabel('Percent Width Change');
legend('Image');

% Plot of percent height change
figure;
plot(taxis , cell2mat(delhgtpcnt), 'o', 'Color',[0 0.75 0.5],...
    'MarkerFaceColor',[0 0.75 0.5], 'MarkerSize',5);
title('Percent Change in Spark Height from Mean Image');
xlabel('Time (s)');
ylabel('Percent Height Change');
legend('Image');

% Format and (optionally) save all figures
quickfigureformatter;

%% Output Run Time

ettot = toc(tv);
fprintf('Total runtime: %5.3f seconds\n\n',ettot)

```

## Bibliography

- [1] Eric J. Jumper and Stanislav Gordeyev. Physics and Measurement of Aero-Optical Effects: Past and Present. *Annual Review of Fluid Mechanics*, 49(1):419–441, January 2017.
- [2] Meng Wang, Ali Mani, and Stanislav Gordeyev. Physics and Computation of Aero-Optics. *Annual Review of Fluid Mechanics*, 44(1):299–321, January 2012.
- [3] Christopher M. Wyckham and Alexander J. Smits. Aero-Optic Distortion in Transonic and Hypersonic Turbulent Boundary Layers. *AIAA Journal*, 47(9):2158–2168, September 2009.
- [4] R. Mark Rennie, David Goorskey, Matthew R. Whiteley, and Eric J. Jumper. Wavefront measurements of a laser-induced breakdown spark in still air. *Applied Optics*, 51(13):2306, May 2012.
- [5] M. Kotzagianni and S. Couris. Femtosecond laser induced breakdown for combustion diagnostics. *Applied Physics Letters*, 100(26):264104, June 2012.
- [6] Eric J. Jumper and Edward J. Fitzgerald. Recent advances in aero-optics. *Progress in Aerospace Sciences*, 37(3):299–339, April 2001.
- [7] David Plemmons, Lance Baxter, Eric Jumper, B. Feather, and R. Wilson. Aero-Optics Effects Testing in AEDC Wind Tunnels. In *24th AIAA Aerodynamic Measurement Technology and Ground Testing Conference*, Portland, Oregon, June 2004. American Institute of Aeronautics and Astronautics.
- [8] Rodney Clark, Michele Banish, and Jay Hammer. Fundamentals of aero-optics phenomena. In *25th Plasmadynamics and Lasers Conference*, Colorado Springs, CO, U.S.A., June 1994. American Institute of Aeronautics and Astronautics.
- [9] Stanislav Gordeyev, Adam E. Smith, Jacob A. Cress, and Eric J. Jumper. Experimental studies of aero-optical properties of subsonic turbulent boundary layers. *Journal of Fluid Mechanics*, 740:214–253, February 2014.
- [10] Stanislav Gordeyev, Mark R. Rennie, Alan B. Cain, and Timothy Hayden. Aero-Optical Measurements of High-Mach Supersonic Boundary Layers. In *46th AIAA Plasmadynamics and Lasers Conference*, Dallas, TX, June 2015. American Institute of Aeronautics and Astronautics.

- [11] Kyle P. Lynch, Russell Spillers, Nathan E. Miller, Daniel Guildenbecher, and Stanislav Gordeyev. Aero-Optical Measurements of a Mach 8 Boundary Layer. In *AIAA AVIATION 2021 FORUM*, VIRTUAL EVENT, August 2021. American Institute of Aeronautics and Astronautics.
- [12] E. R. G. Eckert. Engineering Relations for Heat Transfer and Friction in High-Velocity Laminar and Turbulent Boundary-Layer Flow Over Surfaces With Constant Pressure and Temperature. *Journal of Fluids Engineering*, 78(6):1273–1283, August 1956.
- [13] Daniel Neal, Eric Hedlund, Melissa Lederer, Arnold Collier, Charles Spring, and Bill Yanta. Shack-Hartmann wavefront sensor testing of aero-optic phenomena. In *20th AIAA Advanced Measurement and Ground Testing Technology Conference*, Albuquerque, NM, U.S.A., June 1998. American Institute of Aeronautics and Astronautics.
- [14] W.H. Southwell. Wave-front estimation from wave-front slope measurements. *Journal of the Optical Society of America*, 70(8):998, August 1980.
- [15] Biswajit Pathak and Bosanta R Boruah. Improved wavefront reconstruction algorithm for Shack–Hartmann type wavefront sensors. *Journal of Optics*, 16(5):055403, May 2014.
- [16] Daniel M. Topa. Wavefront reconstruction for the Shack-Hartmann wavefront sensor. page 101, Seattle, WA, September 2002.
- [17] Phan Huy Phuc, Nguyen The Manh, Hyug-Gyo Rhee, Young-Sik Ghim, Ho-Soon Yang, and Yun-Woo Lee. Improved wavefront reconstruction algorithm from slope measurements. *Journal of the Korean Physical Society*, 70(5):469–474, March 2017.
- [18] Stephen M. Anthony and Steve Granick. Image Analysis with Rapid and Accurate Two-Dimensional Gaussian Fitting. *Langmuir*, 25(14):8152–8160, July 2009.
- [19] Alice M. Nightingale and Stanislav Gordeyev. Shack-Hartmann wavefront sensor image analysis: a comparison of centroiding methods and image-processing techniques. *Optical Engineering*, 52(7):071413, March 2013.
- [20] C G Morgan. Laser-induced breakdown of gases. *Reports on Progress in Physics*, 38(5):621–665, May 1975.
- [21] Daniel Neal, Darrell Armstrong, Eric Hedlund, Melissa Lederer, Arnold Collier, Charles Spring, James Gruetzner, Gregory Hebner, and Justin Mansell. Wavefront sensor testing in hypersonic flows using a laser-spark guide star. *Proceedings of the SPIE, Volume 3172*, p. 347-359 (1997), November 1997.
- [22] Mark Rennie, Garnett Cross, David Goorskey, Matthew Whiteley, David Cavalieri, and Eric Jumper. Aero-Optic Measurements Using a Laser-Induced Air Breakdown Beacon. In *40th AIAA Plasmadynamics and Lasers Conference*, San Antonio, Texas, June 2009. American Institute of Aeronautics and Astronautics.

- [23] Mark Rennie, David Cavalieri, Eric Jumper, David Goorskey, Matthew Whiteley, and Garnett Cross. Optical Measurements of a Compressible Shear Layer Using a Laser-Induced Air Breakdown Beacon. In *48th AIAA Aerospace Sciences Meeting Including the New Horizons Forum and Aerospace Exposition*, Orlando, Florida, January 2010. American Institute of Aeronautics and Astronautics.
- [24] R. Mark Rennie, Minh Nguyen, Stanislav Gordeyev, Eric J. Jumper, Alan B. Cain, and Timothy E. Hayden. Wave-Front Measurements of a Supersonic Boundary Layer Using Laser Induced Breakdown. *AIAA Journal*, 55(7):2349–2357, July 2017.
- [25] M. Nguyen, Zareb A. Noel, Jonathan Wells, and R. Mark Rennie. High-order wavefront aberrations due to a laser-induced breakdown spark in still air. *Applied Optics*, 59(25):7510, September 2020.
- [26] R. Rennie, Matthew Whiteley, Eric Jumper, Garnett Cross, and Dave Cavalieri. Measurement of Beacon Anisoplanatism Through a Two-Dimensional Weakly-Compressible Shear Layer. In *39th Plasmadynamics and Lasers Conference*, Seattle, Washington, June 2008. American Institute of Aeronautics and Astronautics.
- [27] Timur A. Labutin, Vasily N. Lednev, Alexey A. Ilyin, and Andrey M. Popov. Femtosecond laser-induced breakdown spectroscopy. *Journal of Analytical Atomic Spectrometry*, 31(1):90–118, 2016.
- [28] Xiao-Long Liu, Xin Lu, Xun Liu, Ting-Ting Xi, Feng Liu, Jing-Long Ma, and Jie Zhang. Tightly focused femtosecond laser pulse in air: from filamentation to breakdown. *Optics Express*, 18(25):26007, December 2010.
- [29] Bo Li, Dayuan Zhang, Jixu Liu, Yifu Tian, Qiang Gao, and Zhongshan Li. A Review of Femtosecond Laser-Induced Emission Techniques for Combustion and Flow Field Diagnostics. *Applied Sciences*, 9(9):1906, May 2019.
- [30] E. L. Gurevich and R. Hergenröder. Femtosecond Laser-Induced Breakdown Spectroscopy: Physics, Applications, and Perspectives. *Applied Spectroscopy*, 61(10):233A–242A, October 2007.
- [31] M. Kotzagianni and S. Couris. Femtosecond laser induced breakdown spectroscopy of air–methane mixtures. *Chemical Physics Letters*, 561-562:36–41, March 2013.
- [32] Anil K. Patnaik, Paul S. Hsu, Adam J. Stolt, Jordi Esteveordal, James R. Gord, and Sukesh Roy. Advantages of Ultrafast LIBS for High-Pressure Diagnostics. In *Imaging and Applied Optics 2018 (3D, AO, AIO, COSI, DH, IS, LACSEA, LS&C, MATH, pCAOP)*, page LW5C.4, Orlando, Florida, 2018. OSA.
- [33] Robert J. Noll. Zernike polynomials and atmospheric turbulence\*. *Journal of the Optical Society of America*, 66(3):207, March 1976.
- [34] Julien Weiss. A Tutorial on the Proper Orthogonal Decomposition. In *AIAA Aviation 2019 Forum*, Dallas, Texas, June 2019. American Institute of Aeronautics and Astronautics.

[35] *Test uncertainty: an american national standard.* ASME, New York, 2006. OCLC: 916340658.